Draft version April 9, 2024
Typeset using LaTeX **twocolumn** style in AASTeX62

Constraining free-free emission and photoevaporative mass loss rates for known proplyds and new VLA-identified candidate proplyds in NGC 1977

Ryan D. Boyden[1, 2, 3, *] and Josh Eisner[3]

[1] *Department of Astronomy, University of Virginia, Charlottesville, VA 22904, USA*
[2] *Space Science Institute, Boulder, CO 80301, USA*
[3] *Steward Observatory, University of Arizona, 933 N. Cherry Ave, Tucson, AZ, 85719, USA*

ABSTRACT

We present Karl G. Jansky Very Large Array observations covering the NGC 1977 region at 3.0, 6.4, and 15.0 GHz. We search for compact radio sources and detect continuum emission from 34 NGC 1977 cluster members and 37 background objects. Of the 34 radio-detected cluster members, 3 are associated with known proplyds in NGC 1977, 22 are associated with additional young stellar objects in NGC 1977, and 9 are newly-identified cluster members. We examine the radio spectral energy distributions, circular polarization, and variability of the detected NGC 1977 sources, and identify 10 new candidate proplyds whose radio fluxes are dominated by optically thin free-free emission. We use measurements of free-free emission to calculate the mass-loss rates of known proplyds and new candidate proplyds in NGC 1977, and find values $\sim 10^{-9} - 10^{-8}$ $M_\odot$ yr^{-1}, which are lower than the mass-loss rates measured towards proplyds in the Orion Nebula Cluster, but consistent with the mass-loss rates predicted by external photoevaporation models for spatially-extended disks that are irradiated by the typical external UV fields encountered in NGC 1977. Finally, we show that photoevaporative disk winds in NGC 1977 may be illuminated by internal or external sources of ionization, depending on their positions within the cluster. This study provides new constraints on disk properties in a clustered star-forming region with a weaker UV environment than the Orion Nebula Cluster, but a stronger UV environment than low-mass star-forming regions like Taurus. Such intermediate UV environments represent the typical conditions of Galactic star and planet formation.

Keywords: open clusters and associations: individual (Orion) — planetary systems — protoplanetary disks — stars: pre-main sequence

1. INTRODUCTION

Most star formation occurs in dense, massive clusters (e.g., Lada et al. 1993; Lada & Lada 2003; Krumholz et al. 2019), and the formation and evolution of planets is likely influenced by the stellar cluster environment. In particular, clusters host massive OB stars that irradiate their surroundings with ultraviolet (UV) photons, and the intense UV radiation from massive stars is capable of heating and dispersing protoplanetary disks through a process known as "external photevaporation" (Winter & Haworth 2022, and references therein). Theoretical work suggests that external photoevaporation can severely reduce the masses, sizes, and lifetimes of disks over a range of realistic disk-cluster conditions (Johnstone et al. 1998; Störzer & Hollenbach 1999; Scally & Clarke 2001; Adams et al. 2004; Clarke 2007; Facchini et al. 2016; Haworth et al. 2018a,b; Winter et al. 2018; Haworth & Clarke 2019; Parker et al. 2021a; Coleman & Haworth 2022; Qiao et al. 2022), which can in turn influence the timescale and building blocks of planet formation (e.g., Throop & Bally 2005; Walsh et al. 2013; Ndugu et al. 2018; Nicholson et al. 2019; Sellek et al. 2020; Haworth 2021; Winter et al. 2022; Boyden & Eisner 2023; Qiao et al. 2023). Indirect evidence for external photoevaporation is also routinely observed in nearby clusters, with surveys finding lower disk fractions near massive OB stars (e.g., Balog et al. 2007; Guarcello et al. 2007; Fang et al. 2012; Guarcello et al. 2016; van Terwisga & Hacar 2023), lower disk masses in clustered vs. lower-mass star-forming regions (e.g., Ansdell et al. 2017; Eisner et al. 2018; van Terwisga et al. 2019, 2020; Maucó et al. 2023), and a lack of spatially extended disks

Corresponding author: Ryan Boyden
rboyden@virginia.edu

* Virginia Initiative on Cosmic Origins Fellow.

in nearby O-star-hosting clusters (e.g., Eisner et al. 2018; Boyden & Eisner 2020; Otter et al. 2021).

The Orion Nebula Cluster (ONC) has long been regarded as the prototypical region for studies of disk evolution in clustered star-formation environments. At a distance of the 400 pc (Hirota et al. 2007; Kraus et al. 2007; Menten et al. 2007; Sandstrom et al. 2007; Kounkel et al. 2017; Großschedl et al. 2018; Kounkel et al. 2018), the ONC hosts several-thousand young ($1-2$ Myr), low-mass (<2 $M_\odot$) stars (Hillenbrand 1997; Fang et al. 2021) that are irradiated by the massive Trapezium stars, most notably the O-star θ^1 Ori C. Compared with other nearby clusters, the ONC contains the largest known population of *proplyds*—disks that are surrounded by cocoons of ionized gas with a cometary morphology. The presence and morphologies of proplyds are a direct result of the external photoevaporation process, in which strong far-ultraviolet (FUV) and extreme-ultraviolet (EUV) radiation from massive stars drive material off the disks in the form of ionized photoevaporative winds (e.g., Johnstone et al. 1998; Störzer & Hollenbach 1999). The high surface brightnesses of the ONC proplyds have enabled large samples of photoevaporating disks in the ONC to be detected and characterized with a range of facilities, including the Very Large Array (e.g., Churchwell et al. 1987; Garay et al. 1987; Zapata et al. 2004a; Forbrich et al. 2016; Sheehan et al. 2016), the Hubble Space Telescope (HST; e.g., O'dell & Wen 1994; Bally et al. 1998, 2000; Ricci et al. 2008) the Atacama Large Millimeter/submillimeter Array (ALMA; e.g., Eisner et al. 2018; Ballering et al. 2023), VLT-MUSE (e.g., Haworth et al. 2023; Aru et al. 2024), and more recently, JWST (e.g., Berné et al. 2022; Habart et al. 2023; McCaughrean & Pearson 2023; Berné et al. 2024).

While studies of the ONC proplyds have provided crucial information on how strong UV fields from massive stars launch photoevaporative winds from the surfaces of circumstellar disks, most stars are born in localized regions of clusters that harbor less extreme irradiation conditions than the proplyd-hosting regions of the ONC. The external UV field strength of a star-forming region is characterized in units of the Habing Field, G_0, where $G_0 = 1.6 \times 10^{-3}$ erg cm^{-2} s^{-1} and is defined as the local ISM FUV field strength over the wavelength range $930 - 2000$ Å (Habing 1968). While disks and proplyds in the ONC are irradiated by intense external FUV fields with typical values $> 10^4 - 10^5$ G_0 (e.g., Johnstone et al. 1998; Störzer & Hollenbach 1999; O'Dell et al. 2017), most stars in the Galaxy, including ones that form in high-mass clusters, are likely irradiated by "intermediate" FUV fields of $\sim 10 - 10^4$ G_0 (e.g., Fatuzzo & Adams 2008; Winter et al. 2020; Parker et al. 2021b; Winter & Haworth 2022), which are weaker than than the FUV fields found in the proplyd-hosting regions of the ONC, but stronger than those found in nearby low-mass star-forming regions like Taurus ($\lesssim 10$ G_0; e.g., Mooley et al. 2013).

The expected prevalence of intermediately-irradiated star-forming environments makes NGC 1977 an ideal region to study Galactic star and planet formation. Located $\sim$0.5° north of the ONC, NGC 1977 hosts several hundred low-mass stars with masses and ages similar to those found in the ONC (Peterson & Megeath 2008; Megeath et al. 2012; Da Rio et al. 2016). Unlike other nearby star-forming clusters in Orion, the most massive stars in NGC 1977 are B-type stars rather than O-type stars. This means that as disk-bearing stars evolve in NGC 1977, they are never exposed to the extreme $10^4 - 10^5$ G_0 UV fields found in the intensely-irradiated regions of the ONC, and are instead irradiated by $\sim 10 - 10^4$ G_0 UV fields that mirror the UV environments of typical Galactic star-forming regions. The absence of $> 10^4$ G_0 UV fields in NGC 1977 also marks an important distinction from disks currently located in the intermediately-irradiated outskirts of the ONC, as dynamical evolution implies that these disks were likely closer to the massive Trapezium stars and, thus, exposed to stronger UV fields in the past than they are now (e.g., Scally & Clarke 2001; Winter et al. 2019).

Recently, Bally et al. (2012) and Kim et al. (2016) discovered ~ 10 candidate proplyds in NGC 1977 with similar morphologies as the ONC proplyds. This discovery confirms that intermediate UV fields are sufficient to trigger external photoevaporation in planet-forming disks, as predicted by external photoevaporation theory (e.g., Adams et al. 2004; Clarke 2007; Facchini et al. 2016; Haworth et al. 2018a,b; Haworth & Clarke 2019). However, the HST observations used to discover the NGC 1977 proplyds only mapped a small area of NGC 1977, so it remains unclear whether external photoevaporation is truly a widespread phenomenon in the intermediately-irradiatedly environment of NGC 1977.

Here we present new NSF's Karl G. Jansky Very Large Array (henceforth denoted as VLA) observations that have mapped the entire NGC 1977 region at 3.0 GHz (13 cm), 6.4 GHz (4.6 cm), and 15.0 GHz (2.0 cm). At long centimeter wavelengths, dust emission from protoplanetary disks declines significantly due to its steep spectral index ($F_\nu \propto \nu^{2+\beta}$, $\beta \approx 0 - 2$), and when there is substantial ionized gas, free-free emission dominates the continuum. Centimeter wavelength observations can therefore be used to identify which disk-bearing stars

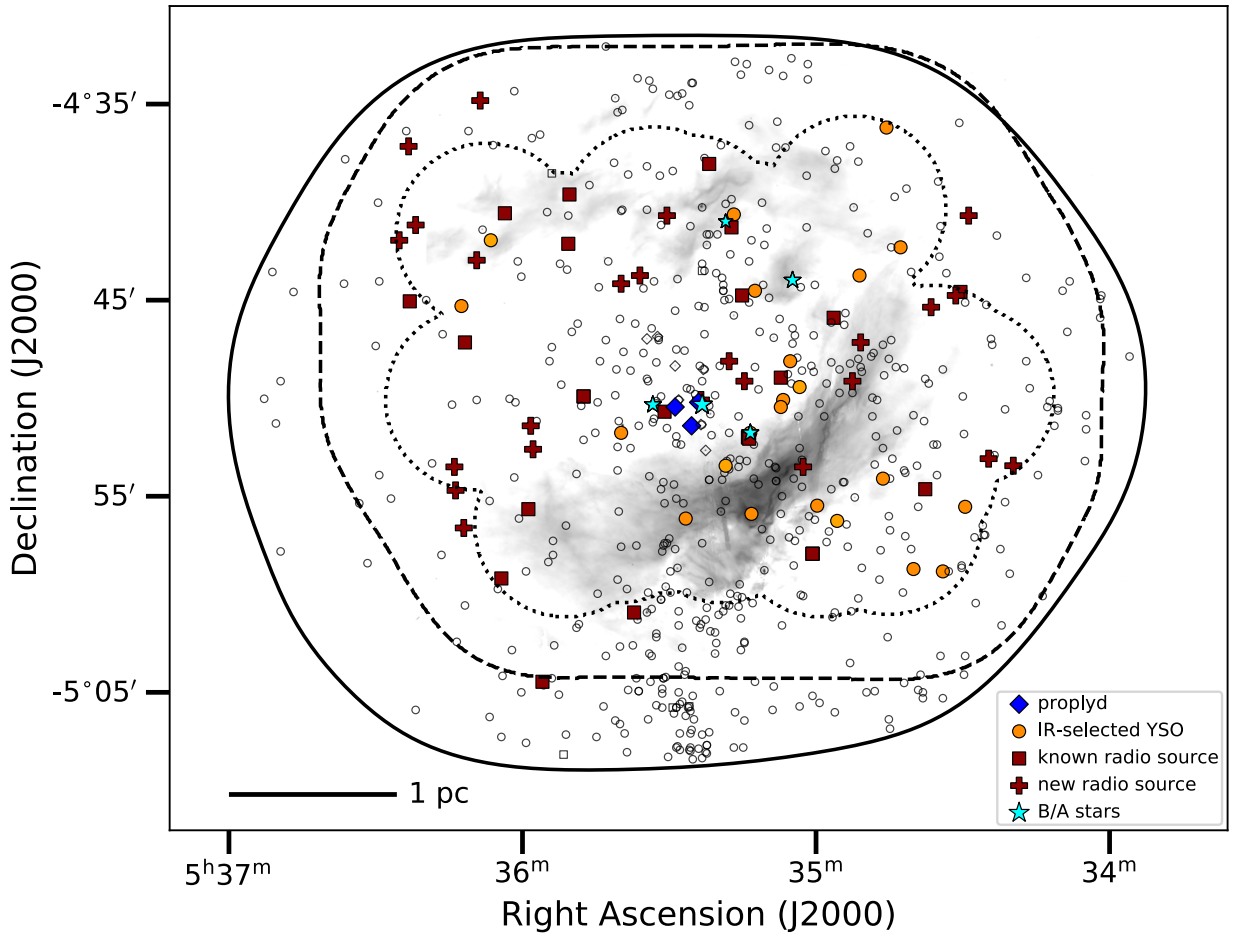

Figure 1. The NGC 1977 region, as seen at 8 μm with *Spitzer*-IRAC (grayscale). Solid, dashed, and dotted contours depict the field of views of our 3.0, 6.4, and 15.0 GHz VLA observations, respectively (see Section 3). The positions of 42 Ori (∼B1V star), HD 37058 (∼B3V star), HD 294264 (∼B3V star), HD 369658 (∼B3V star), and HD 294262 (∼A0 star) are marked with cyan stars, with larger star sizes corresponding to earlier spectral types. Our VLA maps cover ∼600 sources previously identified at optical, infrared, and/or radio wavelengths (see Section 2), and we detect a total of 71 sources. We use diamond markers to indicate the positions of known proplyds in NGC 1977 (Bally et al. 2012; Kim et al. 2016), circle markers to indicate the positions of infrared-selected YSOs (Peterson & Megeath 2008; Megeath et al. 2012; Da Rio et al. 2016), and square markers to denote the positions of known radio sources (Kounkel et al. 2014). Filled diamonds, circles, and squares correspond to sources that are detected in our maps, while open diamonds, circles, and squares correspond to nondetected sources. Finally, we use plus symbols to denote the positions of sources that are detected in our maps but not associated with the proplyd, YSO, and known radio source catalogs.

in a clustered star-forming region are launching ionized winds driven by external photoevaporaton. With our deep, multi-band VLA observations, we can search for free-free-emitting proplyds in NGC 1977, and establish a sample of intermediately-irradiated young stellar objects (YSOs) that are influenced by external photoevaporation.

2. SAMPLE

The NGC 1977 region comprises several-hundred pre-main-sequence stars ranging from brown dwarfs to B-type stars (see review in Peterson & Megeath 2008). Figure 1 shows the spatial distribution of YSOs in NGC 1977. The lower-mass cluster members are distributed throughout all of NGC 1977, while the higher-mass B- and A-type stars are concentrated towards the inner regions of the cluster. In particular, the B1V star 42 Ori is located at the cluster center along with the B3V stars HD 37058 and HD 294264; and, the B3V star HD 36958 and A0 double star HD 294262 lie to the northwest of 42 Ori.

Here we assemble catalogs that can be used to identify radio emission from known sources in NGC 1977. Our first catalog consists of all 10 NGC 1977 proplyds that were identified by Bally et al. (2012) and Kim et al. (2016) with HST and/or *Spitzer* imaging. The positions of these proplyds are indicated in Figure 1 with diamond markers. All 10 proplyds are located in the same inner region of NGC 1977, as the bulk of them were identified with HST observations that mapped a small area to the

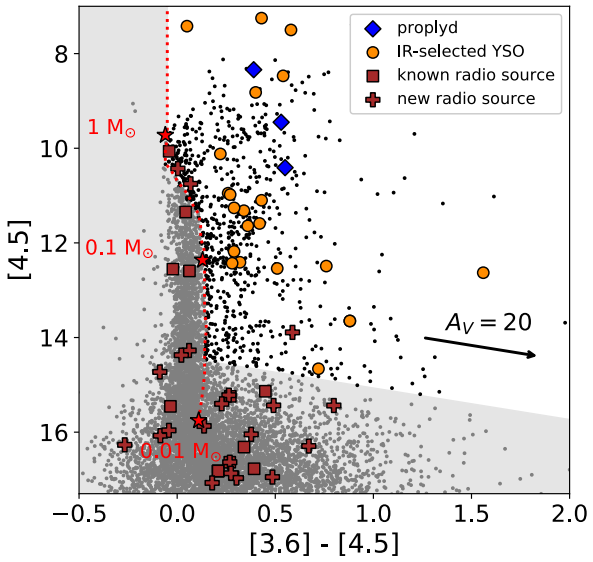

Figure 2. Color-magnitude diagram for sources detected in our VLA maps and all *Spitzer* point sources within our VLA maps. Photometric data for VLA detections previously classified as YSOs are taken from Megeath et al. (2012). Photometric data for unclassified radio detections and additional *Spitzer* point sources are taken from the online *Spitzer* point source catalog. The dotted red line shows the 1 Myr isochrone for the pre-main-sequence evolutionary models from Baraffe et al. (2015), while the red star symbols indicate the individual model points for a 0.01 $M_\odot$ star, a 0.1 $M_\odot$ star, and a 1 $M_\odot$ star. The solid black arrow shows the extinction vector for $A_V = 20$. The shaded gray region indicates the region of color-magnitude magnitude space where we classify VLA-detected sources as candidate background objects (c.f., Gutermuth et al. 2008; Harvey et al. 2008; Gutermuth et al. 2009; Megeath et al. 2012). If a *Spitzer* point source falls within the shaded grey region, we use a filled gray circle to plot its position. Otherwise, we plot its position using a filled black circle. For the VLA-detected sources, we plot their positions using the same marker symbols as in Figure 1.

east of 42 Ori. One of the proplyds, however, lies outside of the region mapped with HST, but this source (identified with *Spitzer* imaging, see Kim et al. 2016) is located directly north of 42 Ori, and is therefore positioned in the inner region of NGC 1977.

Our second catalog consists of all infrared-selected YSOs within the central $\sim 30' \times 45'$ region of NGC 1977. This includes 85 disk-bearing stars detected at 24 μm with *Spitzer*-MIPS (Peterson & Megeath 2008), 291 YSOs detected at H-band with SDSS-APOGEE (Da Rio et al. 2016), and 386 *Spitzer*-selected YSOs from the photometric catalog of Megeath et al. (2012), for a total of 559 unique sources after accounting for overlap amongst the different infrared catalogs. In Figure 1, we use circle markers to indicate the positions of all infrared-selected YSOs in our VLA maps.

To obtain updated source coordinates for the infrared-selected YSOs, we use Gaia DR3 (Gaia Collaboration et al. 2022). Namely, we search the Gaia archive for objects within 1.″5 of the published source coordinates, finding matches for $\sim$ 90% of the considered sources. The updated coordinates from Gaia show a systematic offset of around $-1''$ to $-0.''5$ in right ascension and $-0.''25$ to $-0.''75$ in declination from the published *Spitzer* catalog coordinates (Peterson & Megeath 2008; Megeath et al. 2012). They also show a similar offset in right ascension but a smaller, $-0.''25$ to $0''$ offset in declination from the published SDSS-APOGEE catalog coordinates (Da Rio et al. 2016). We use these systematic offsets to extrapolate the coordinates of the $\sim$ 10% of sources without GAIA counterparts onto the GAIA reference frame. In particular, we apply an offset of $0.''75$ in right ascension and $0.''5$ in declination to the coordinates of *Spitzer*-selected objects, and an offset of $0.''5$ in right ascension to the coordinates of SDSS-APOGEE selected objects.

The *Spitzer* point source catalog[1] contains thousands of additional sources that fall within the central $\sim 30' \times 45'$ region of NGC 1977. However, most of these are background objects not associated with NGC 1977. Figure 2 shows a color-magnitude diagram for all *Spitzer* point sources in NGC 1977 with available photometry at 3.6 and 4.5 μm. The *Spitzer* point sources are color-coded by their location in color-magnitude space, with black points denoting sources that are consistent with being YSOs, and gray points denoting sources that are consistent with being background objects. We consider a *Spitzer* point source to be a contaminant background source if it has *Spitzer*-band colors that are bluer than the expected colors of a $\sim$1 Myr-old pre-main-sequence star (and thus, inconsistent with infrared excess), or if it has *Spitzer*-band magnitudes that are fainter than the expected magnitude of a $\sim$1 Myr-old YSO with a mass $>$0.05 $M_\odot$ (consistent with previous YSO classification schemes; e.g., Gutermuth et al. 2008; Harvey et al. 2008; Gutermuth et al. 2009; Megeath et al. 2012). To determine the expected colors and magnitudes for $>$0.05 $M_\odot$ YSOs, we use the 1 Myr isochrone from the pre-main-sequence evolutionary models of Baraffe et al. (2015), shown in Figure 2, and we assume a distance of 400 pc.

While our selection criteria for YSOs versus background objects may reject potential sub-stellar objects in NGC 1977, they are sufficient to identify YSOs with

[1] https://irsa.ipac.caltech.edu/Missions/spitzer.html

Table 1. Summary of VLA observations

Band	Obs. Type	Date	rms (μJy)	Peak rms (μJy)	Beam size	Beam P.A. (°)
3.0 GHz	Mosaic	2021 September 29	27	$\sim$150	$1\farcs5 \times 2\farcs3$	16
6.4 GHz	Mosaic	2021 September 29	24	$\sim$130	$1\farcs0 \times 1\farcs5$	-27
15.0 GHz	Individual Pointings	2021 September 29	30	$\sim 20 \times 10^3$	$0\farcs3 \times 0\farcs5$	-7

disks, which are the main objects of interest in this study. Under these criteria, we classify the majority of *Spitzer* point sources as background objects (see Figure 2). Of the remaining sources that are not classified as background objects, most are objects that have been previously classified as YSOs by Megeath et al. (2012). Some, however, are consistent with YSOs in two or three photometric bands, but lack photometric coverage in additional *Spitzer* bands due to contaminating nebulosity and/or local extinction effects. These candidate YSOs are not associated with the Megeath et al. (2012) catalog, which only includes YSOs with photometric coverage in four or more bands.

Finally, we consider the catalog of 40 known radio sources that fall within the NGC 1977 region and were detected previously at 4.5 and/or 7.5 GHz by Kounkel et al. (2014). Most of these radio sources have *Spitzer* point source counterparts whose photometry are consistent with background objects under our selection criteria. A small subset, however, has two-, three-, or four-band photometry that is consistent with a YSO, while another subset has counterparts in one of more of the previously-assembled YSO catalogs for NGC 1977. In Figures 1 and 2, we use square markers to plot sources associated with the Kounkel et al. (2014) radio source catalog; however, if a source is associated with both the Kounkel et al. (2014) catalog and our YSO catalog, we plot its position with the same circle markers used to denote YSOs.

3. OBSERVATIONS AND DATA REDUCTION

We imaged the NGC 1977 cluster at 3.0 GHz (13 cm), 6.4 GHz (4.6 cm), and 15.0 GHz (2.0 cm) with the VLA. Observations were taken on 2021 September 29 under project code 21A-015. At this date, the VLA was in its B-configuration, which provided baselines ranging from 0.21 km to 11.1 km.

Table 1 provides an overview of our multi-wavelength VLA dataset, and in Figure 1, we show the field of views of our observations at each wavelength. The 15.0 GHz observations consisted of 46 individual pointings that were centered on the positions of the known proplyds and the 24 μm-selected YSOs in NGC 1977 (see Section 2), which was sufficient to cover the majority of additional NGC 1977 sources in our search catalogs (see Figure 1). At 3.0 and 6.4 GHz, the primary beams are wide enough such that large portions of NGC 1977 can be mosaicked efficiently. We utilized 10 pointings at 3.0 GHz and 66 pointings at 6.4 GHz to mosaic the central $\sim 30' \times 45'$ region of NGC 1977 over these frequencies, and we employed a hexagonal mosaic pattern with a pointing spacing of FWHM/$\sqrt{3}$ in order to achieve Nyquist sampling across these maps.

The spectral setups at each observing wavelength were designed to maximize sensitivity to continuum emission. Observations at 3.0 GHz were taken using the VLA's S-band receivers, with 8 subbands arranged continuously from 1.988 - 4.012 GHz for a total bandwidth of 2 GHz. The 6.4 GHz data were taken using the VLA's C-band receivers. We centered two 2 GHz basebands at 5.25 GHz and 7.5 GHz in order to avoid strong radio-frequency interference (RFI) in the range 4.0 - 4.2 GHz from satellites in the Clarke Belt, and the 16 128 MHz subbands in each baseband were arranged from 4.226 - 6.724 GHz and 6.7467-8.534 GHz to provide a bandwidth of 4 GHz. For the 15.0 GHz observations, we utilized the VLA's Ku-band receivers. The 64 128 MHz subbands available at Ku-band were arranged from 11.756 - 18.412 GHz. Most of the data between 12-12.8 GHz and 17.2-17.6 GHz were, however, were affected by significant RFI, so the 15.0 GHz observations achieved an effective bandwidth of around 5 GHz.

All observations were reduced using the VLA continuum data reduction pipeline, which included procedures for automatic and manual flagging of RFI as well as standard flux, bandpass, and gain calibrations. The bright quasar J0319+4130 was used to derive bandpass solutions for each antenna. To calculate antenna-based complex gains, we used periodic observations of J0503+0203 for observations at 3.0 GHz, and J0541-0541 for observations at 6.4 and 16.0 GHz. Moreover, 3C147 was used as the flux density calibrator for observations at 3.0 and 6.4

Table 2. Catalog Associations of Detected Sources

Catalog	No. Sources[a]	No. Detections[b]
Proplyd catalogs	10	3
Full YSO catalog[c]	559	24
Spitzer 24μm YSO catalog (P08)	85	5
SDSS-APOGEE YSO catalog (D16)	291	17
Full Spitzer YSO catalog (M12)	386	12
Known radio sources (K14)	40	27
New radio sources[d]	...	24
All VLA-detected sources		71
Confirmed/Candidate NGC 1977 sources		34
Background sources		37

Notes: References for proplyd catalogs: Bally et al. (2012); Kim et al. (2016). Reference for Spitzer 24 μm catalog: Peterson & Megeath (2008), i.e., "P08". Reference for Spitzer SDSS-APOGEE catalog: Da Rio et al. (2016), i.e., "D16". Reference for Spitzer YSO catalog: Megeath et al. (2012), i.e., "M12". Reference for known radio source catalog: Kounkel et al. (2014), i.e., "K14".

[a] Indicates all sources covered within our VLA maps.

[b] Indicates all detections in our VLA maps.

[c] Indicates all unique YSO sources in our maps after accounting for overlap amongst the P08, M12, and D16 catalogs.

[d] Indicates all radio detections not associated with a proplyd, YSO, or known radio source catalog.

GHz, and 3C48 was used as the flux density calibrator for observations at 15.0 GHz.

We imaged the radio-continuum observations using the CASA `tclean` task in MFS (Multi-Frequency Synthesis) mode. The 3.0 and 6.4 GHz mosaics were imaged with a phase center of 05:35:23.16 -4:50:18.09, i.e., the coordinates of 42 Ori. For the 15.0 GHz observations, we imaged the individual fields separately out to a primary beam value of 0.001, and then generated smaller sub-images towards the positions of individual sources using the closest field pointing. Clean boxes were determined using an iterative process where we first placed clean boxes around all objects detected above 10σ, generated a cleaned image, searched the residuals for detections above 5σ, and then generated a new cleaned image with additional clean boxes placed around all additional detections. For our final cleaned images, we used the "mtmfs" (Multi-Term Multi-Frequency Synthesis; Rau & Cornwell 2011) clean algorithm with nterms = 2, a Briggs weighting method with a robust parameter of 0.5, and a *uv* cut of >25 kλ. The *uv* cut was employed to spatially filter extended emission in NGC 1977 and improve the noise levels in the vicinity of compact radio sources. Our chosen *uv* cut of >25 kλ eliminated spatial scales >8″.

Our main 3.0, 6.4, and 15.0 GHz image products were generated in the Stokes I plane using a mosaic gridder for the 3.0 and 6.4 GHz observations, and a standard gridder for the 15.0 GHz observations. To search for signatures of circular polarization towards VLA-detected sources (see Section 4.3), we also generated an additional set of 3.0, 6.4, and 15.0 GHz images in the Stokes V plane following the same cleaning procedure outlined above. We used the awproject gridder to generate the Stokes V images, as this gridder corrects for beam squinting and allows for a more reliable examination of Stokes V signals that are spatially offset from a pointing center (see EVLA memo 113). Finally, to improve the spectral characterization of a few VLA-detected sources, we also imaged 5.25 and 7.5 GHz C-band basebands separately (see Section 4.2).

The synthesized beam sizes of our final cleaned images are 1.″5 × 2.″3 at 3.0 GHz, 1.″0 × 1.″5 at 6.4 GHz, and 0.″3 × 0.″5 at 15.0 GHz (see Table 1). At the 400 pc distance to Orion, these beam sizes correspond to spatial resolutions of about ∼120 AU, ∼400 AU, and ∼600 AU, respectively.

4. RESULTS

4.1. *Source Detections*

To identify compact radio sources in NGC 1977, we first perform a blind detection search over the full Stokes I VLA images. Our maps contain a large number of synthesized beams ($> 10^7$), and so we must employ a conservative noise threshold to ensure that none of the blindly-detected sources are noise spikes. However, if a source is blindly detected at multiple wavelengths, then the probability that the detection is a noise spike would decrease. We therefore use an $>8\sigma$ detection limit for sources that are blindly detected at a single wavelength, which ensures that <<1 of the detections are Gaussian noise spikes. For blind detections over multiple wavelengths, we use a lower detection threshold of $>6\sigma$, at which level <<1 Gaussian noise spikes are expected at the same position in multiple images.

We also perform a detection search towards the predetermined positions of all sources from the proplyd, YSO, and known radio source catalogs that we compiled in Section 2. We limit our catalog search radius to 1″, reflective of the typical positional uncertainties of sources without GAIA counterparts, as well as the expected sizes of ionized proplyd structures in NGC 1977 (e.g., Kim et al. 2016). Due to the smaller number of

synthesized beams being probed in our catalog search versus our blind detection search, we are also able to employ a lower detection threshold in our catalog search. We adopt a $>3.5\sigma$ detection threshold for the YSO and known radio source catalog searches at 3.0 and 6.4 GHz, as we expect $<<1$ Gaussian noise spikes above this level. For the proplyd catalog search, we employ a lower detection threshold of $>2.5\sigma$ at 3.0 and 6.4 GHz, as $<<1$ Gaussian noises spikes are still expected at this threshold for a catalog search of 10 objects. For the 15.0 GHz catalog searches, we use a detection threshold of $>3.75\sigma$ due to the larger number of beams probed at 15.0 GHz versus 3.0 GHz or 6.4 GHz. However, we relax the 15.0 GHz detection threshold down to $>3.5\sigma$ if the source is also detected in 3.0 GHz or 6.4 GHz, following the discussion above.

The rms noise is calculated from a 120×120 pixel box around each pixel in the residual map. The 3.0 and 6.4 GHz images typically have local rms levels of $\sim 25 - 35$ μJy, while regions closer to the image outskirts and/or the bright radio source J053558.88-045537.7 have rms levels of around $\sim$100 μJy (see Table 1). For the 15.0 GHz images, the rms levels vary from $\sim$30 μJy to $\sim$30 mJy depending of the position of a source relative to a 15.0 GHz pointing center. All of the sources in our proplyd catalog have 15.0 GHz rms levels of $\sim 30 - 40$ μJy, and towards the full sample of cataloged sources that fall within the field of view of our 15.0 GHz maps (see Figure 1), $\sim$50% have 15.0 GHz rms levels $<$50 μJy, $\sim$66% have 15.0 GHz rms levels $<$70 μJy, and $\sim$80% have 15.0 GHz rms levels $<$1 mJy.

Figure 1 shows the positions of all detected sources in our maps. We detect a total of 71 distinct objects through our blind and catalog searches. Of these 71 objects, 56 are detected at 3.0 GHz, 65 are detected at 6.4 GHz, and 26 are detected at 15.0 GHz.

Table 2 summarizes the catalog associations of the detected sources. 25 of the 71 detections are associated with an infrared-selected YSO, and 3 of these radio-detected YSOs are also associated with known proplyds in NGC 1977. The remaining detections in our sample are either known radio sources in our VLA maps (27 of the 71 detections), or sources that are identified from our blind detection search but not associated with the proplyd, YSO, or known radio source catalogs (24 of the 71 detections). Of the 27 known radio sources detected in our maps, 5 are associated with an infrared-selected YSO.

In Figure 3, we show radial profiles of the spatial distributions of sources detected in our VLA maps. The detection rate among infrared-selected YSOs is low ($\sim 5 - 10$%), but we see a slight increase in the overall detection rate towards the cluster center. The detection rate among known proplyds is also low ($\sim$30%), but here the dependence on projected separation is even steeper than what is seen towards the infrared-selected YSOs. For the 46 radio-detected sources that are not associated with a proplyd or YSO catalog, we initially see an increase in the number of detections at larger projected separations. However, towards the outskirts of our maps, the rms noise is higher, and so we see a decline in the number of these detections at projected separations $\gtrsim 15'$.

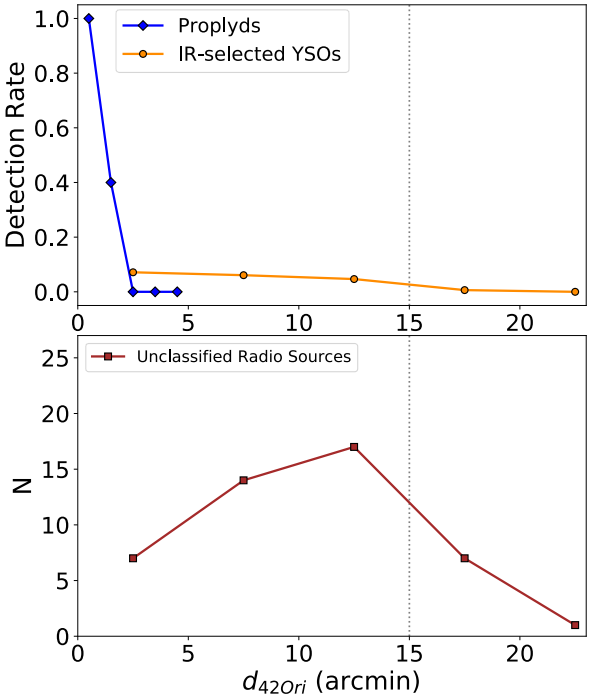

Figure 3. Top: Radially-averaged detection fractions observed towards the HST- and Spitzer-identified proplyd catalog (blue) and the infrared-selected YSO catalog (orange, see Section 2), plotted as a function of projected separation from 42 Ori. We use $1'$ bins to compute the detection rates for the proplyd catalog, and $5'$ bins to compute the detection rates for the YSO catalog. The gray dotted line depicts the approximate primary beam full-width-at-half maximum of our 6.4 GHz VLA mosaic. Bottom: Radially-averaged spatial distribution of radio sources that are detected in our VLA maps but not associated with a known proplyd or YSO catalog (i.e., "Unclassified Radio Sources").

Table 3. Properties of VLA-detected sources in NGC 1977

ID	R.A. (J2000)	Decl. (J2000)	Catalog	F_ν, 3.0 GHz (mJy)	F_ν, 6.4 GHz (mJy)	F_ν, 15.0 GHz (mJy)	Radio Classification	Notes
(1)	(2)	(3)	(4)	(5)	(6)	(7)	(8)	(9)
1	05:35:24.10	–4:50:09.60	KCFF1, P08, D16, M12	0.023 ± 0.102	-0.001 ± 0.086	0.109 ± 0.038	Known Proplyd	
2	05:35:25.52	–4:51:20.65	KCFF2, P08, D16, M12	0.108 ± 0.030	0.121 ± 0.025	-0.029 ± 0.129	Known Proplyd	E, P
3	05:35:28.82	–4:50:22.60	KCFF3, P08	-0.001 ± 0.104	0.061 ± 0.024	0.043 ± 0.131	Known Proplyd	
4	05:36:06.42	–4:41:53.83	P08, D16, M12	0.050 ± 0.114	0.106 ± 0.023	0.062 ± 0.124	Possible Proplyd	E
5	05:35:03.26	–4:49:21.00	P08, D16, M12	0.021 ± 0.095	0.073 ± 0.022	0.128 ± 0.037	Candidate Jet	PS
6	05:35:18.38	–4:53:23.55	P08, D16, M12	0.004 ± 0.111	0.051 ± 0.025	-0.035 ± 0.124	Possible Proplyd	O
7	05:34:55.67	–4:56:12.22	P08, D16, M12, K14	0.007 ± 0.125	0.028 ± 0.088	0.243 ± 0.043	Possible Jet	
8	05:34:45.55	–4:36:07.69	D16	0.241 ± 0.072	0.471 ± 0.049	68.052 ± 85.217	Candidate Jet	PS
9	05:35:16.77	–4:40:32.53	D16	0.497 ± 0.049	0.766 ± 0.058	0.710 ± 0.147	Candidate Proplyd	FS, NP
10	05:34:42.68	–4:42:14.69	D16, K14	0.108 ± 0.039	0.143 ± 0.024	-0.670 ± 3.296	Possible Proplyd	E, V
11	05:34:51.06	–4:43:41.46	D16	0.091 ± 0.032	0.133 ± 0.024	-0.176 ± 1.677	Possible Proplyd	
12	05:35:12.46	–4:44:25.93	D16, K14	0.232 ± 0.033	0.372 ± 0.028	0.513 ± 0.113	Candidate Jet	PS
13	05:35:05.25	–4:48:02.89	D16	0.097 ± 0.028	0.218 ± 0.025	0.244 ± 0.043	Candidate Proplyd	FS
14	05:35:07.24	–4:50:25.51	D16	0.125 ± 0.030	0.120 ± 0.025	0.214 ± 0.041	Candidate Jet	PS
15	05:35:39.74	–4:51:41.68	D16	0.533 ± 0.050	1.912 ± 0.138	1.846 ± 0.142	Candidate Proplyd	E, FS, NP
16	05:34:46.41	–4:54:02.02	D16, K14	0.216 ± 0.035	0.553 ± 0.046	0.405 ± 0.056	Candidate Proplyd	FS, NP
17	05:35:13.10	–4:55:52.47	D16, M12	0.042 ± 0.125	0.138 ± 0.027	0.166 ± 0.277	Possible Proplyd	O
18	05:35:26.59	–4:56:06.78	D16	0.047 ± 0.128	0.167 ± 0.026	0.183 ± 0.223	Possible Proplyd	
19	05:34:40.14	–4:58:39.91	D16	0.079 ± 0.166	0.284 ± 0.034	2.521 ± 0.466	Protostar	E, SS
20	05:36:12.40	–4:45:15.88	M12	0.386 ± 0.042	0.299 ± 0.028	-13.030 ± 20.212	Candidate Proplyd	FS
21	05:35:06.79	–4:50:01.98	M12	0.279 ± 0.035	0.276 ± 0.030	0.087 ± 0.161	Candidate Proplyd	E, FS
22	05:35:13.34	–4:51:44.94	M12, K14	0.038 ± 0.117	0.118 ± 0.030	0.261 ± 0.346	Radio Star	P, V
23	05:34:59.89	–4:55:27.32	M12, K14	0.220 ± 0.037	0.064 ± 0.083	0.553 ± 0.060	Candidate Jet	E, PS
24	05:34:29.56	–4:55:30.20	M12	0.111 ± 0.046	0.018 ± 0.099	3.840 ± 8.691	Possible Radio Star	
25	05:34:34.08	–4:58:49.89	M12	0.213 ± 0.056	0.144 ± 0.030	-1.732 ± 11.525	Possible Proplyd	
26	05:35:17.21	–4:41:13.50	K14 †	0.010 ± 0.114	0.087 ± 0.022	0.181 ± 0.223	Radio Star	V
27	05:35:15.12	–4:44:42.90	K14 †	0.217 ± 0.033	0.317 ± 0.031	0.274 ± 0.051	Candidate Proplyd	E, FS, V
28	05:34:56.33	–4:45:48.80	K14 †	0.162 ± 0.031	0.135 ± 0.024	0.112 ± 0.124	Possible Jet	E, FS, P, V
29	05:34:37.64	–4:54:36.00	K14 †	0.622 ± 0.057	0.716 ± 0.056	0.878 ± 0.084	Candidate Jet	E, PS, P, V
30	05:36:21.86	–4:41:06.34	··· †	0.259 ± 0.054	0.280 ± 0.043	-0.016 ± 12.587	Possible Proplyd	
31	05:35:39.82	–4:44:04.48	··· †	0.035 ± 0.102	0.309 ± 0.031	0.265 ± 0.052	Candidate Proplyd	FS
32	05:34:52.55	–4:49:06.45	··· †	0.273 ± 0.034	0.265 ± 0.029	0.195 ± 0.044	Candidate Proplyd	FS
33	05:35:23.55	–4:50:01.25	··· †	0.223 ± 0.034	0.160 ± 0.027	0.137 ± 0.151	Candidate Proplyd	FS
34	05:35:02.76	–4:53:27.73	··· †	0.209 ± 0.033	0.273 ± 0.030	-0.065 ± 1.099	Candidate Jet	E, PS

Notes. Column (1): source IDs used in this article. Columns (2) and (3): phase center coordinates. Column (3): catalog association of VLA-detected sources. Sources with HST- and/or Spitzer-identified proplyds are indicated using the full IDs assigned by Kim et al. (2016), which consists of a "KCFF" followed by an additional digit. Sources detected at 24 μm with *Spitzer*-MIPS (Peterson & Megeath 2008) are labeled with a "P08". Sources detected at *H*-band with SDSS-APOGEE (Da Rio et al. 2016) are labeled with a "D16." An "M12" is used to specify association with the full catalog of *Spitzer*-selected YSOs from Megeath et al. (2012). A "K14" is used to specify associations with the radio catalog of Kounkel et al. (2014). Sources not associated with any of the above catalogs are indicated with an ellipses. Columns (5), (6), and (7): measured fluxes at 3.0 GHz, 6.4 GHz, and 15.0 GHz. Column (8): Source classification, based on the observed properties of the detected radio emission (see Section 4.5). Column (9): Notes on the morphologies, radio spectral energy distributions (SEDs), polarization, and/or variability characteristics of individual sources. 'E' and 'O' correspond to notes related to source morphology, with 'E' denoting sources with spatially resolved and elongated radio emission in one or more bands, and 'O' denoting sources with radio emission that is spatially offset from the central star (see Section 4.1.2). 'FS', 'PS', and 'SS' correspond to notes related to the radio spectral indices, with 'FS' denoting flat spectrum sources with SEDs consistent with optically thin free-free emission, 'PS' denoting positive spectrum sources with SEDs consistent with optically thick free-free emission, and 'SS' denoting steep spectrum sources with SEDs consistent with dust emission (see Section 4.2). 'P' and 'NP' correspond to notes related to circular polarization, with 'P' denoting sources with detected Stokes V emission above 2.5σ and measured circular polarization fractions >10%, and 'NP' denoting sources that are not detected in the Stokes V plane but have Stokes V upper limits that imply a circular polarization fraction of <10% (see Section 4.3). Finally, a 'V' is used to denote sources with variable 6.4 GHz emission, based on comparisons with prior flux measurements from Kounkel et al. (2014) (see Section 4.4).

† Indicates a candidate cluster member (see Section 4.1).

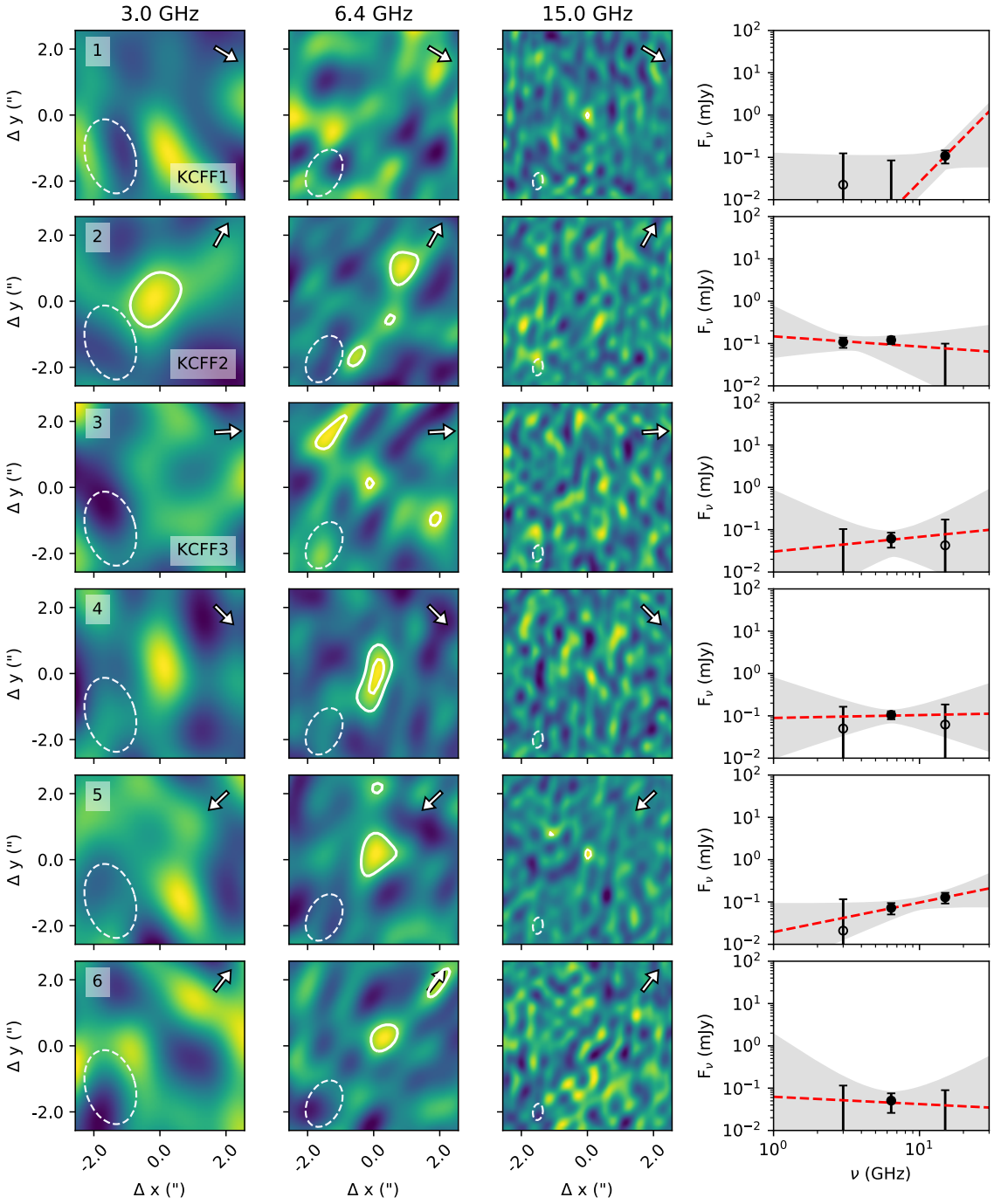

Figure 4. 3.0 GHz (S-band) continuum images (left column), 6.4 GHz (C-band) continuum images (center left column), 15.0 GHz (Ku-band) continuum images (center right column), and radio spectral energy distributions (SEDs, right column) of NGC 1977 sources detected in our VLA maps. Each row shows the continuum images and SED of a single source, with our source ID (see Table 3) provided in the top-left corner of each 3.0 GHz image panel. For detections with optically identified proplyds, we include the proplyd name from Kim et al. (2016) in the bottom right corner of the 3.0 GHz image panel. The white arrow in each image panel points to the direction of the nearest (in projected separation) B- or A-type star in NGC 1977. The solid white contours in the 3.0 and 6.4 GHz image panels show 2.5σ to 10.5σ emission in increments of 2σ. In the 15.0 GHz panels, the solid white contours show 3.5σ to 11.5σ emission in increments of 2σ. The dashed white contour in each panel shows the synthesized beam at each wavelength. In the SED panels, filled black circles show the fluxes measured with Gaussian fitting when a source is detected above our noise threshold, while open black circles indicate fluxes measured in an aperture around the source position when the source not detected above our noise threshold. If a detection has prior radio-continuum flux measurements from Kounkel et al. (2014), we show them in the SED panel as blue squares. The red dashed lines show the best-fit single power law or piecewise free-free emission power law that is derived for each source (see Section 4.2). The shaded gray regions show the 1σ confidence intervals of each fit. For sources that are modeled with a piecewise power law, we include red circles in the SED panels that show the the 5.25 and 7.5 GHz fluxes that are obtained when imaging the two 6.4 GHz basebands separately (see Section 3).

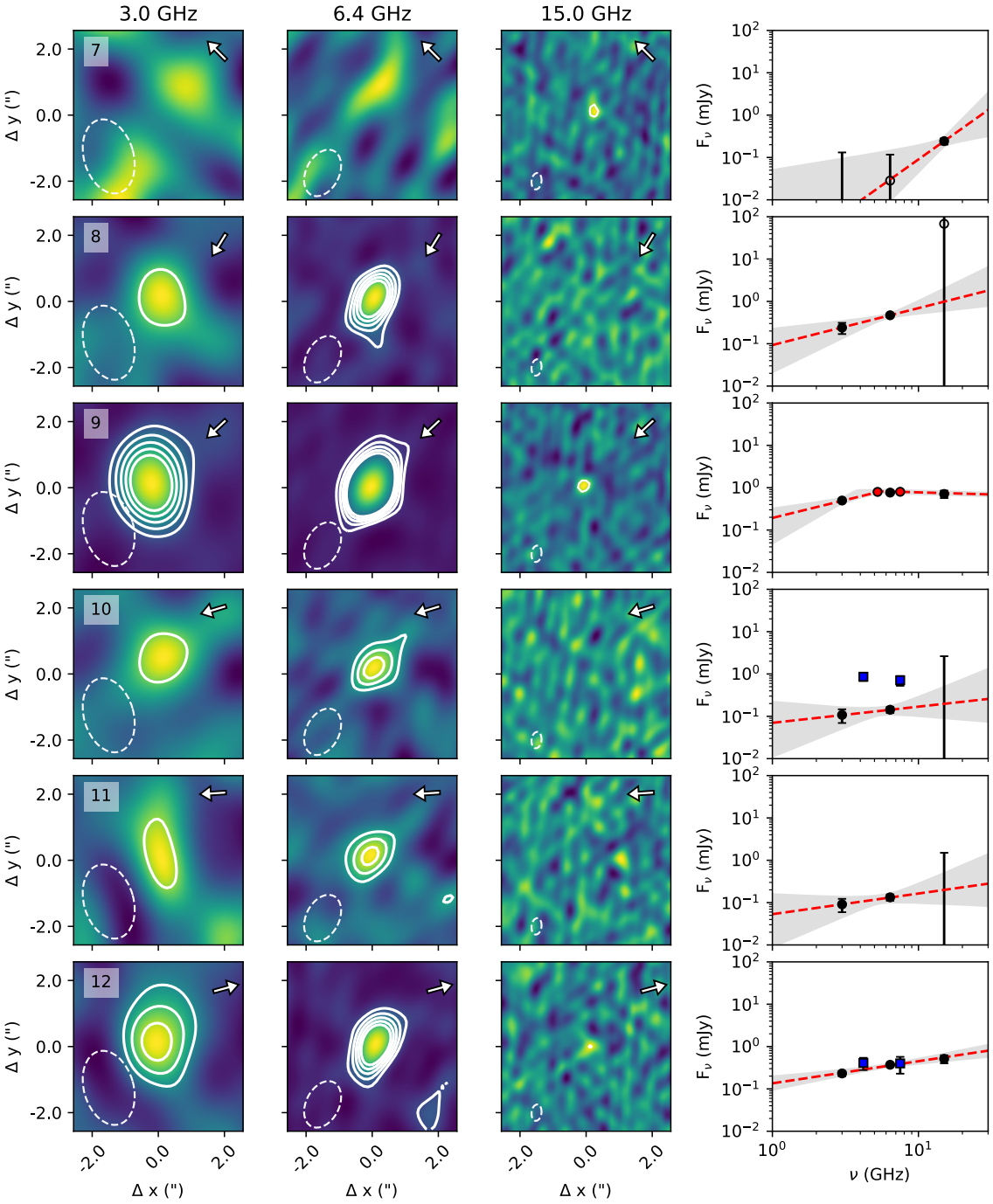

Figure 5. Continuation of Figure 4.

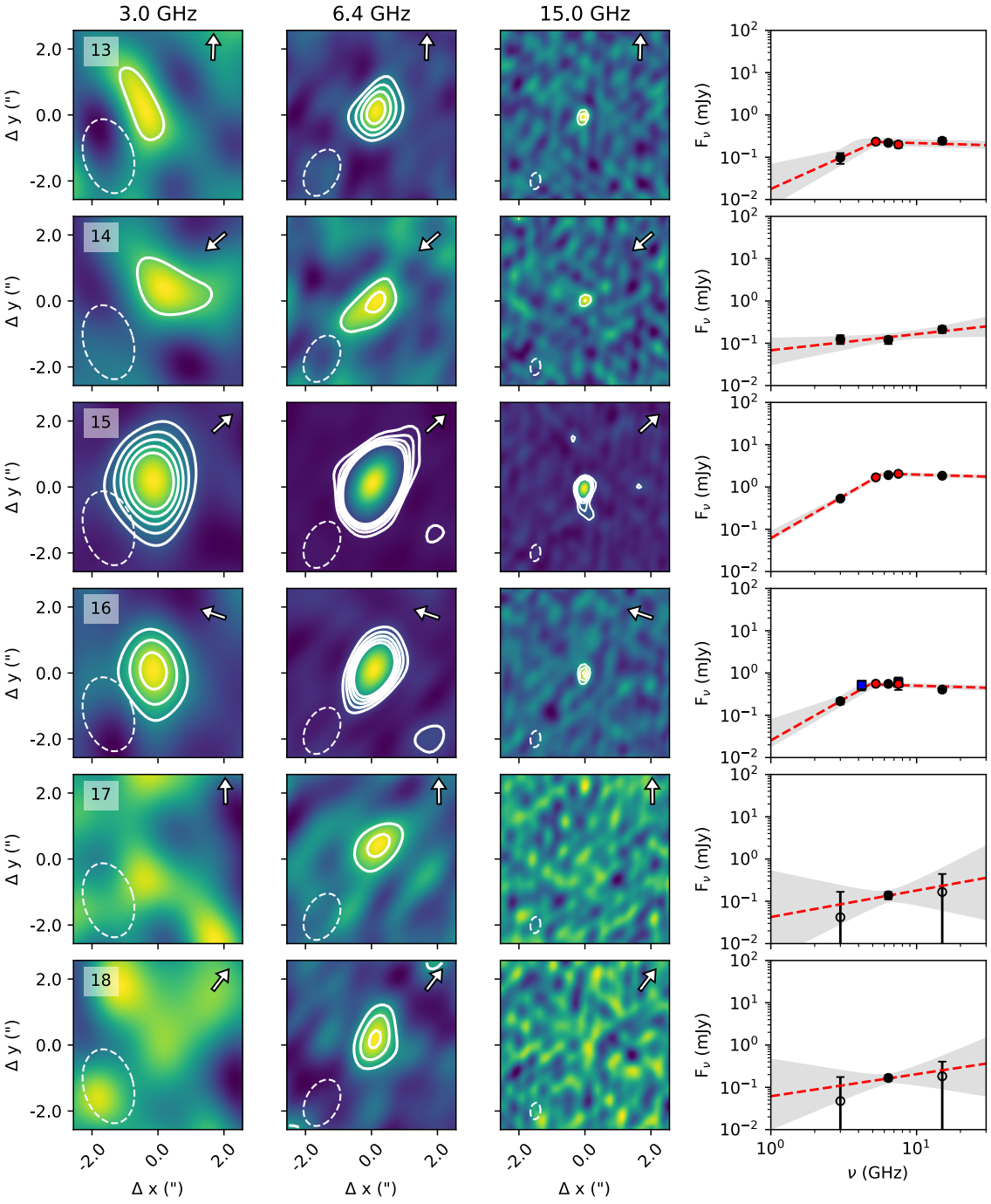

Figure 6. Continuation of Figure 4.

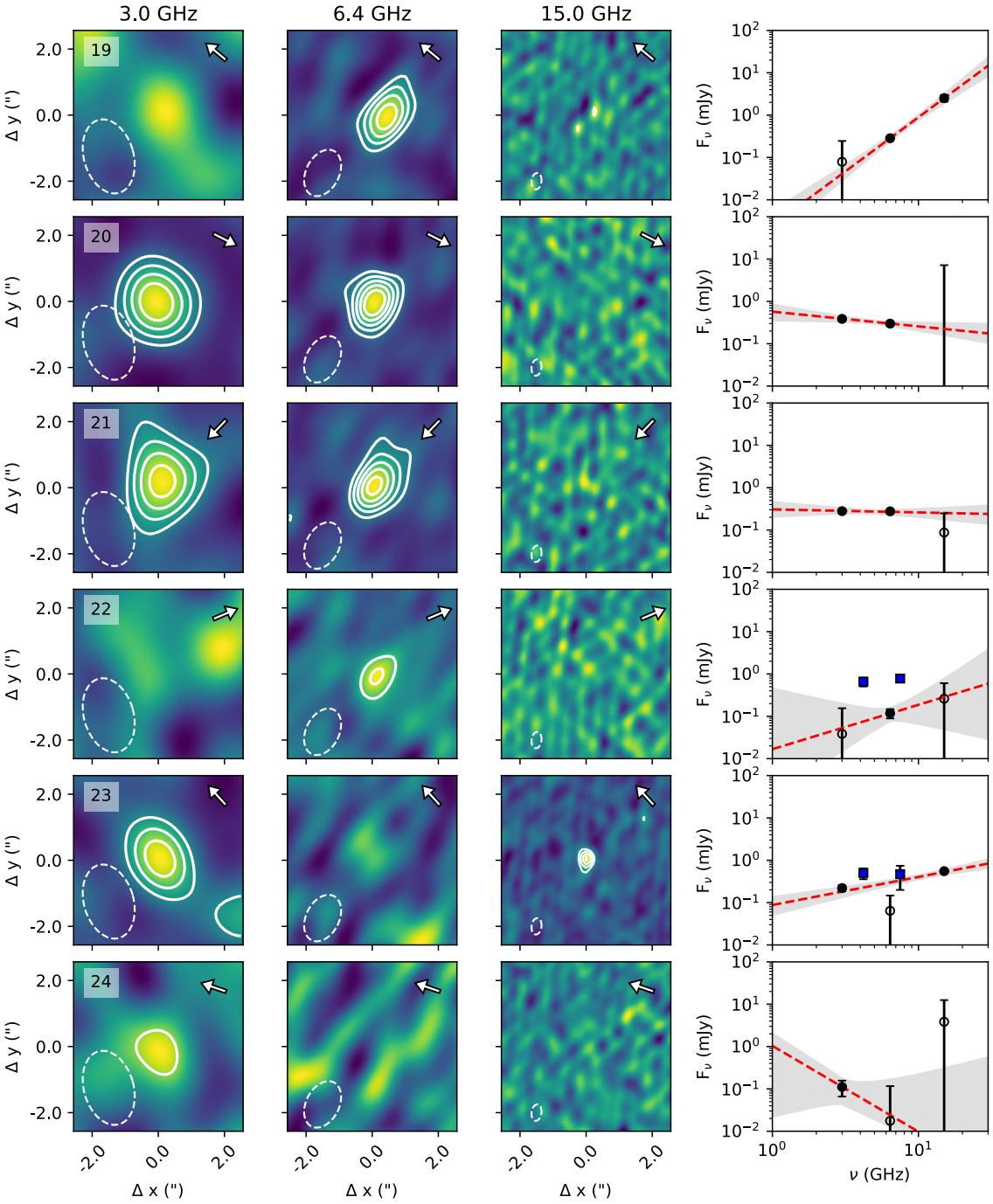

Figure 7. Continuation of Figure 4.

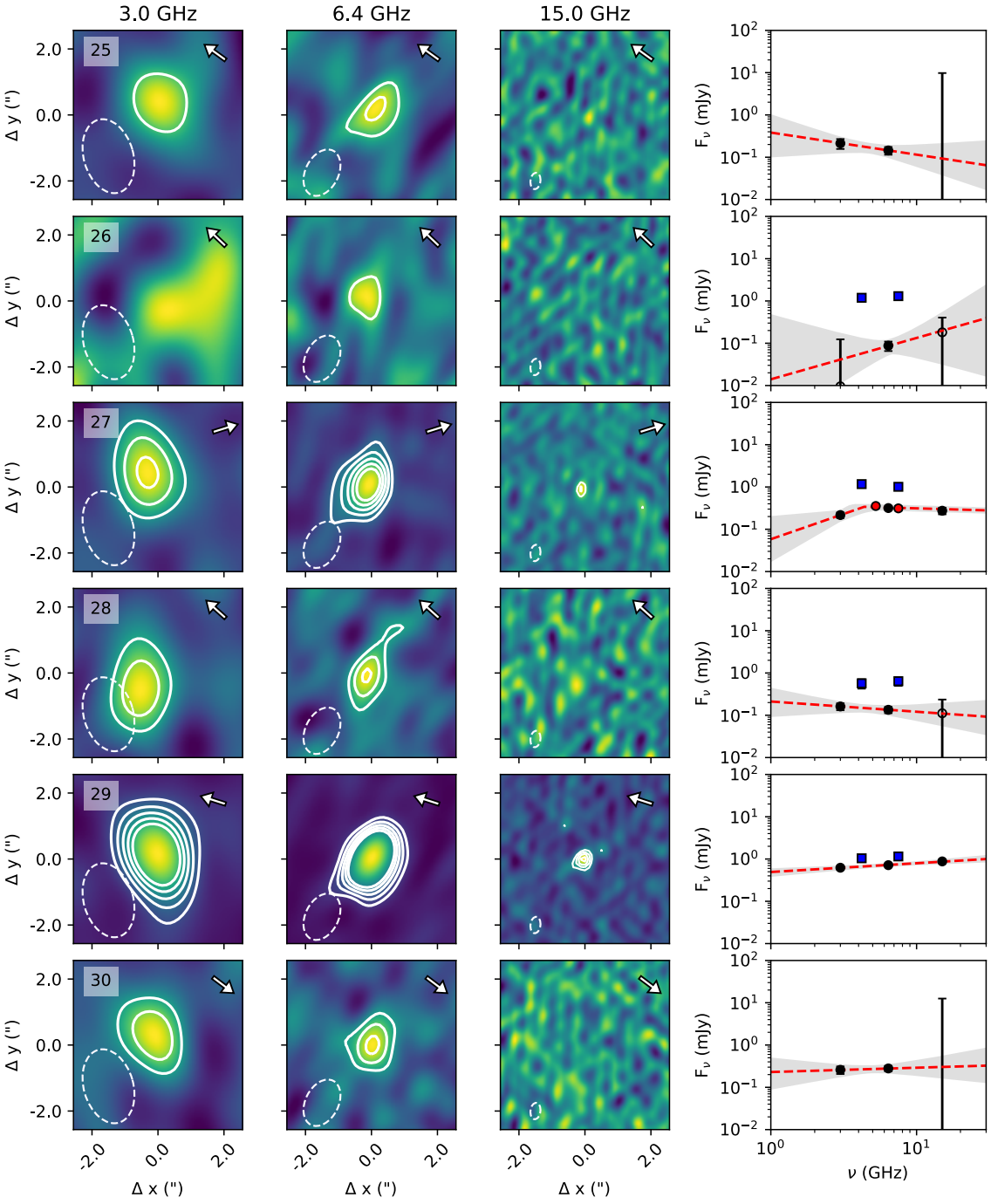

Figure 8. Continuation of Figure 4.

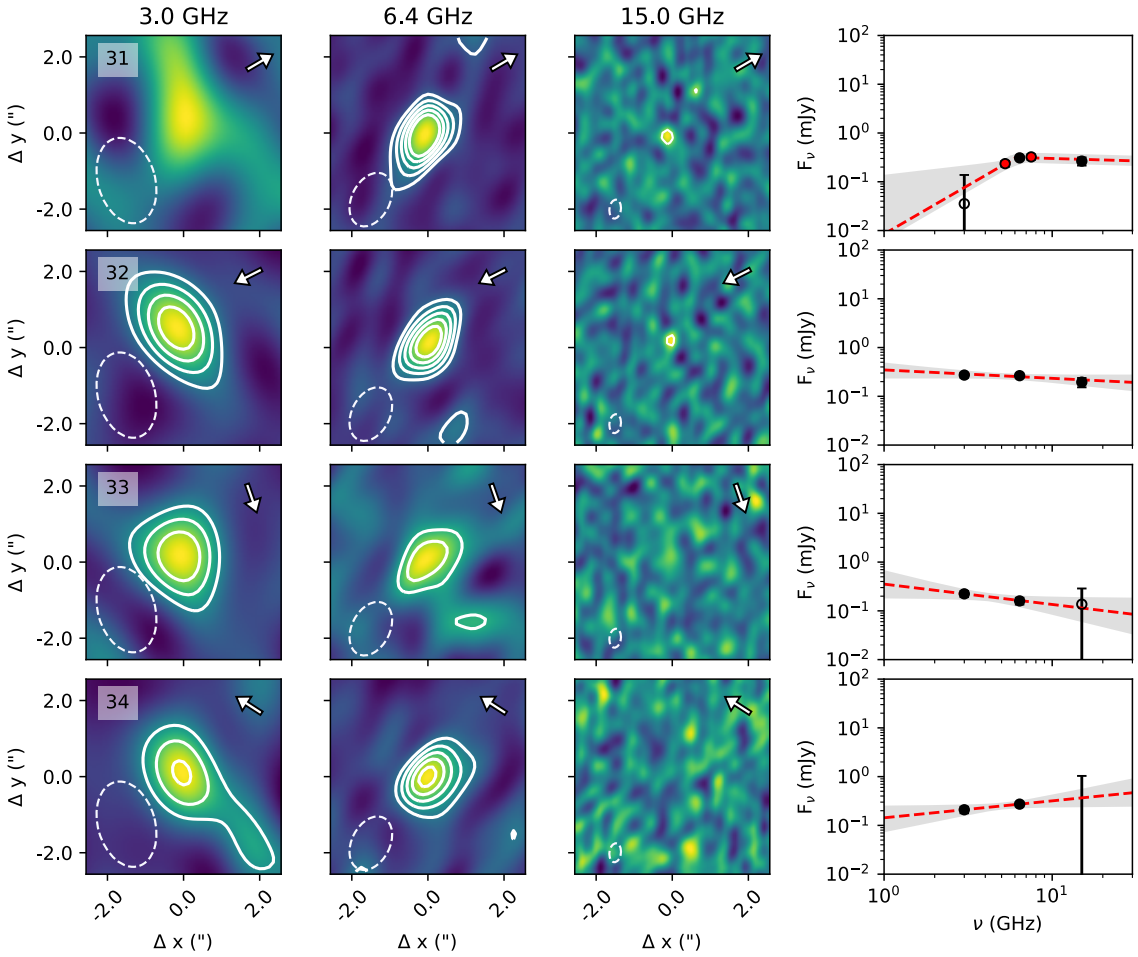

Figure 9. Continuation of Figure 4.

We use the *Spitzer* point source catalog to determine whether the 46 uncataloged radio detections are contaminant background objects or candidate cluster members of NGC 1977. 37 of them have *Spitzer* counterparts with photometry that are consistent with background objects (see Figure 2), and are thus likely to not be associated with NGC 1977. We classify these 37 sources as probable background objects, and provide further discussion on their observed properties in Appendix A. The remaining 9 uncataloged detections either have GAIA parallaxes that imply a distance of 400 pc, or *Spitzer* point source counterparts that have partial photometric coverage but are consistent with YSOs under two- or three-band selection criteria (see Section 2). We consider these 9 sources to be newly-detected cluster members of NGC 1977, and we include them with our samples of radio-detected proplyds and YSOs, for a total of 34 radio-detected NGC 1977 sources.

We measure the fluxes of all detected sources by fitting a 2D Gaussian to the observed radio emission using the CASA task `imfit`. If a source is not detected in all radio-continuum bands, then we use aperture photometery to obtain an unbiased signal estimate towards the source position in each non-detected band. We also include an additional 5% error on all flux measurements to account for the uncertainty in the absolute flux scale. Table 3 lists the measured fluxes at 3.0 GHz, 6.4 GHz, and 15.0 GHz for all 34 radio-detected sources that we identify as confirmed or candidate NGC 1977 cluster members, along with the source IDs, coordinates, and individual catalog associations of each source. For the remainder of this paper, we use the source IDs listed in Table 3 when describing individual NGC 1977 sources, unless otherwise noted.

In Figures 4 - 9, we show 3.0 GHz subimages, 6.4 GHz subimages, 15.0 GHz subimages, and radio spectral energy distributions (SEDs) for the 34 VLA-detected NGC 1977 cluster members. Each row shows the results for an individual detected source. The sub-images have dimensions of $\sim 2'' \times 2''$, and the SEDs are produced using the continuum flux measurements provided in Table 3. However, if a detection is a known radio source associated with the Kounkel et al. (2014) catalog, we include the cm-wavelength flux measurements from Kounkel et al. (2014) in the SED panels.

4.1.1. *Proplyd Detections*

We detect cm-wavelength emission towards the positions of proplyds KCFF1, KCFF2, and KCFF3 in our VLA maps. In Table 3, these proplyds correspond to source IDs 1, 2, and 3, respectively. All three proplyds are located within $\sim 1\farcm4$ of 42 Ori (see Figure 1), and they were initially discovered by Kim et al. (2016), who identified KCFF1 in archival *Spitzer*/*IRAC* images, and KCFF2 and KCFF3 in archival HST/ACS 658N images.

In Figure 10, we show *Spitzer* 8μm observations of KCFF1 and HST 658N images of KCFF2 and KCFF3. We also show contours of the measured radio-continuum emission measured towards these sources in order to compare the morphologies of the detected radio emission with the morphologies seen in the *Spitzer* and HST images. The *Spitzer* observations of KCFF1 are obtained from the Spitzer Heritage Archive[2] (IRSA 2022), and the HST/ACS images of KFCC2 and KCFF3 are obtained from the MAST archive[3]. We also register the *Spitzer* and HST images to the 2MASS coordinate system using the `astrometry.net` software package (Lang et al. 2010). After registration to the 2MASS coordinate system, the astrometric uncertainties between our radio-wavelength images and the the HST and/or *Spitzer* images are $\lesssim 0.2''$ (e.g., Eisner et al. 2005).

The multi-wavelength images shown in Figure 10 reveal that our VLA observations are tracing the bright "heads" of each proplyd. Towards the position of KCFF3, the detected 6.4 GHz emission is marginally resolved along the direction of the proplyd head, revealing a morphology at cm-wavelengths that is nearly identical to the morphology seen in the HST image. Towards KCFF1, we see a similar pattern with the detected 15.0 GHz emission, although the Spitzer observations of KCFF1 have a much coarser angular resolution than the 15.0 GHz observations, so the detected cm emission appears very compact in Figure 10. For KCFF2, the detected 3.0 GHz emission is concentrated towards the proplyd head, but some of the detected 6.4 GHz emission is spatially offset from the proplyd head. The 6.4 GHz emission measured towards KCFF2 may therefore be tracing both an ionized jet and a proplyd head, similar to what is observed towards a subset of ONC proplyds (e.g., Bally et al. 1998, 2000; Ricci et al. 2008).

4.1.2. *Structured detections*

11 of the 34 radio-detected NGC 1977 sources are marginally resolved in our 3.0, 6.4, and/or 15.0 GHz maps: sources 2, 4, 10, 15, 19, 21, 23, 27, 28, 29, and 34. These sources are labeled as resolved detections in Table 3. Resolved detections are identified through a combination of single and multiple Gaussian fitting. If a VLA-detected source has centrally concentrated emission that is well-described by a single Gaussian, then we consider it to be resolved if the fitted Gaussian size is

[2] https://sha.ipac.caltech.edu/applications/Spitzer/SHA/
[3] https://mast.stsci.edu/portal/Mashup/Clients/Mast/Portal.html

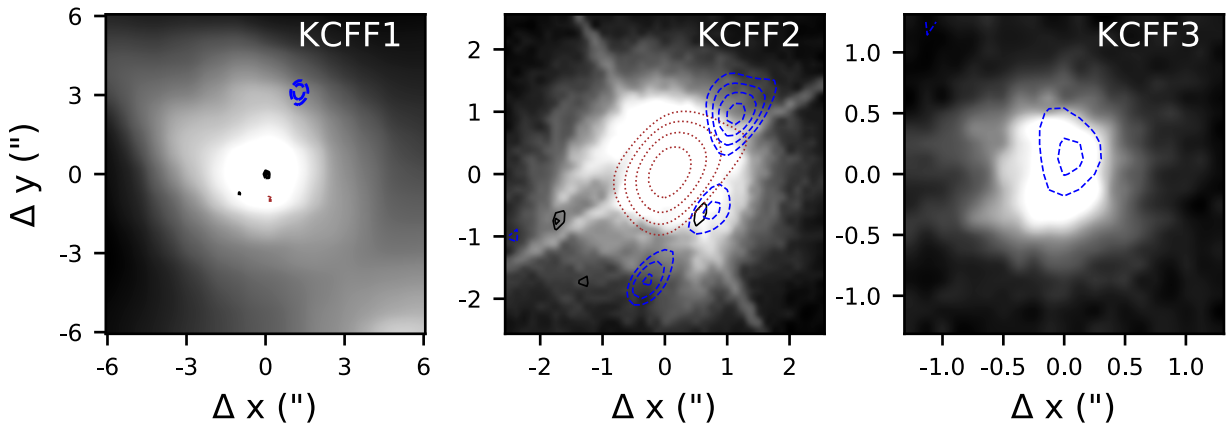

Figure 10. Spitzer 8 μm image (left) and HST/ACS F658N images (center and right) of known proplyds detected in our VLA maps. Contours show VLA radio-continuum emission measured towards the positions of the proplyds, with dotted brown contours showing 3.0 GHz emission, dashed blue contours showing 6.4 GHz emission, and solid black contours showing 15.0 GHz emission. All contours start start at 2σ and increase in increments of 0.5σ. The HST and Spitzer images are registered with respect to the 2MASS coordinate system. The (0, 0) coordinates for KCFF1 are: 5:35:24.10 –4:50:09.60. The (0, 0) coordinates for KCFF2 are: 5:35:25.51 –4:51:20.65. Finally, the (0, 0) coordinates for KCFF3 are 5:35:28.82 –4:50:22.60.

larger than the synthesized beam, following the criteria outlined in Otter et al. (2021). If a source has extended emission that is not well-encapsulated by a single Gaussian, then we perform single and multiple Gaussian fits to the detected emission and consider the source to be resolved if none of the single-Gaussian fits are within the derived confidence intervals.

We also find that sources 6 and 17 have unresolved emission that is spatially offset from the central stellar coordinates by $\sim 0\farcs3 - 0\farcs5$. These two sources are all detected in the 6.4 GHz continuum band only, and they are labeled as spatially offset detections in Table 3.

Some of the marginally resolved detections have elongated morphologies that are oriented towards the direction of a nearby B- or A-type star and suggestive of ionized proplyd structures, including sources 15, 21, and 34. For the spatially offset detections, the offset radio emission is closer to a B- or A-type star than the central star, consistent with the expected orientations of proplyds. Despite these suggestive proplyd morphologies, it is worth noting that at our current resolution ($\sim 0\farcs5 - 1\farcs0$), the observed morphologies of the resolved and offset detections can also be explained by jets with disk orientations that are perpendicular to the direction of a nearby B- or A-type star (Rodriguez et al. 1994; Carrasco-González et al. 2012; Tychoniec et al. 2018a; Tobin et al. 2020). Hence, from a spatial examination of our VLA maps alone, it is challenging to determine whether the marginally resolved or spatially offset detections are winds or jets.

4.2. *Radio Spectral Energy Distributions*

Ionized gas from photoevaporating disks, stellar winds, and outflows can emit strong free-free emission at centimeter wavelengths (e.g., Wendker et al. 1973; Garay et al. 1987; Felli et al. 1993a; Plambeck et al. 1995; Anglada et al. 1998; Reipurth et al. 1999). For a spherically symmetric wind or collimated jet, the free-free emission spectrum is expected to follow a power-law dependence with the piecewise form:

$$F_\nu = \begin{cases} F_{\nu_{\rm turn}} \left(\frac{\nu}{\nu_{\rm turn}}\right)^{-0.1} & \nu \geq \nu_{\rm turn} \\ F_{\nu_{\rm turn}} \left(\frac{\nu}{\nu_{\rm turn}}\right)^{\alpha} & \nu < \nu_{\rm turn} \end{cases} \quad (1)$$

(e.g., Panagia & Felli 1975; Wright & Barlow 1975; Reynolds 1986). Here, $\nu_{\rm turn}$ is the turnover frequency above which the ionized gas is optically thin, $F_{\nu_{\rm turn}}$ is the flux density at $\nu_{\rm turn}$, and α is the spectral index of the optically thick component of the ionized gas. Depending on the density, geometry, ionization structure, and velocity of the outflow, α is expected to be a positive number between 0 to 2 (for examples, see Reynolds 1986).

The turnover frequency is sensitive to the size and density at the inner boundary where the ionized material is launched, with denser and smaller inner boundaries resulting in higher turnover frequencies. Ionized jets from low- and high-mass protostars are thought to have turnover frequencies above 50 GHz (Anglada et al. 2018, and references therein), since large samples of jets are observed to be optically thick at radio wavelengths (e.g., Anglada et al. 1998; Tychoniec et al. 2018b). Ionized disk winds have more extended spatial origins than

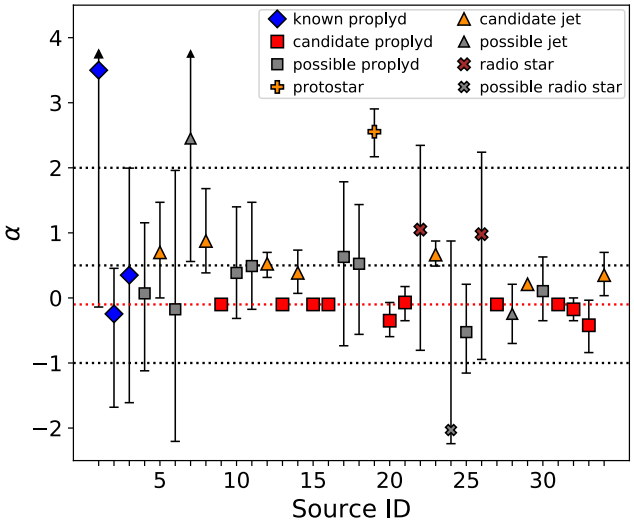

Figure 11. Radio spectral indices derived for each VLA-detected NGC 1977 cluster member. For piecewise-power-law-modeled sources, we plot the inferred spectral index above the best-fit turnover frequency, i.e., $\alpha = -0.1$. All sources are color- and symbol-coded source following their radio classifications in Table 3. The red dotted line depicts $\alpha = -0.1$, the expected spectral index of optically thin free-free emission. The dotted black lines show $\alpha = -1$, $\alpha = -0.5$, and $\alpha = 2$.

jets, so the free-free emission spectrum of a disk wind usually turns over and becomes optically thin at lower frequencies (e.g., Eisner et al. 2008; Pascucci et al. 2012; Owen et al. 2013; Pascucci et al. 2014). In the ONC, the majority of free-free emitting proplyds have turnover frequencies below ∼10 GHz (e.g., Sheehan et al. 2016).

Here we measure the spectral indices of all VLA-detected NGC 1977 sources to discriminate between optically thin free-free emission from a wind, optically thick free-free emission from a wind or jet, or emission from other mechanisms. We initially measure the spectral indices by fitting a power law to the radio SEDs. The power law model has two free parameters: the spectral index and the reference flux at a particular frequency. We generate a large suite of power law models over a broad range of spectral indices and reference fluxes, and we fit these models to the measured 3.0, 6.4, and 15.0 GHz radio fluxes via a χ^2 minimization procedure. Since a few of the detections show signs of radio variability (see Section 4.4), we opt to use our radio flux measurements alone in the fitting procedure.

Most of our sources are fit quite well by a single power law model, but a subset shows evidence of having a free-free turnover within the frequency range covered by our observations (e.g., sources 9, 15, 16). We construct a piecewise free-free emission model via Equation 1 and

Table 4. Radio spectral energy distribution modeling results

ID	Model	$F_{\nu,\,\mathrm{ref}}$ (mJy)	α	ν_{turn} (GHz)	Notes
(1)	(2)	(3)	(4)	(5)	(6)
1	Single Power Law	$1.222^{0.628}_{1.161}$	> -0.14		
2	Single Power Law	$0.064^{0.199}_{0.062}$	$-0.24^{0.70}_{1.44}$		
3	Single Power Law	$0.100^{0.777}_{0.097}$	$0.35^{1.64}_{1.96}$		
4	Single Power Law	$0.113^{0.450}_{0.098}$	$0.07^{1.08}_{1.19}$		
5	Single Power Law	$0.211^{0.247}_{0.133}$	$0.70^{0.77}_{0.70}$		PS
6	Single Power Law	$0.034^{0.513}_{0.033}$	$-0.17^{2.14}_{2.03}$		
7	Single Power Law	$1.328^{2.120}_{1.013}$	>0.56		
8	Single Power Law	$1.825^{4.688}_{1.051}$	$0.88^{0.81}_{0.49}$		PS
9	Piecewise Power Law	$0.824^{0.080}_{0.073}$	$0.85^{1.15}_{0.35}$	$5.52^{1.31}_{1.89}$	FS
10	Single Power Law	$0.260^{1.068}_{0.186}$	$0.39^{1.02}_{0.70}$		
11	Single Power Law	$0.282^{1.121}_{0.200}$	$0.49^{0.98}_{0.66}$		
12	Single Power Law	$0.807^{0.302}_{0.244}$	$0.53^{0.17}_{0.21}$		PS
13	Piecewise Power Law	$0.231^{0.042}_{0.032}$	$1.55^{0.45}_{0.85}$	$5.23^{1.60}_{1.46}$	FS
14	Single Power Law	$0.253^{0.152}_{0.103}$	$0.39^{0.35}_{0.31}$		PS
15	Piecewise Power Law	$2.073^{0.118}_{0.148}$	$2.00^{0.00}_{0.25}$	$5.81^{0.44}_{0.15}$	FS
16	Piecewise Power Law	$0.539^{0.041}_{0.056}$	$1.95^{0.05}_{0.80}$	$4.79^{0.87}_{0.58}$	FS
17	Single Power Law	$0.362^{1.649}_{0.324}$	$0.63^{1.15}_{1.37}$		
18	Single Power Law	$0.367^{1.076}_{0.304}$	$0.53^{0.91}_{1.08}$		
19	Single Power Law	$14.729^{8.518}_{6.374}$	$2.56^{0.35}_{0.38}$		SS
20	Single Power Law	$0.174^{0.124}_{0.070}$	$-0.35^{0.28}_{0.25}$		FS
21	Single Power Law	$0.242^{0.140}_{0.105}$	$-0.07^{0.25}_{0.28}$		FS
22	Single Power Law	$0.595^{3.203}_{0.567}$	$1.05^{1.30}_{1.86}$		
23	Single Power Law	$0.841^{0.223}_{0.203}$	$0.66^{0.21}_{0.17}$		PS
24	Single Power Law	$0.001^{0.562}_{0.001}$	$-2.03^{2.90}_{0.21}$		
25	Single Power Law	$0.064^{0.175}_{0.047}$	$-0.52^{0.74}_{0.63}$		
26	Single Power Law	$0.393^{1.948}_{0.376}$	$0.98^{1.26}_{1.93}$		
27	Piecewise Power Law	$0.340^{0.040}_{0.047}$	$1.20^{0.80}_{0.90}$	$4.35^{2.77}_{1.02}$	FS
28	Single Power Law	$0.092^{0.128}_{0.057}$	$-0.24^{0.46}_{0.46}$		FS
29	Single Power Law	$1.007^{0.182}_{0.142}$	$0.21^{0.10}_{0.07}$		PS
30	Single Power Law	$0.328^{0.501}_{0.197}$	$0.11^{0.53}_{0.46}$		
31	Piecewise Power Law	$0.315^{0.057}_{0.053}$	$2.00^{0.00}_{1.60}$	$6.10^{3.79}_{0.73}$	FS
32	Single Power Law	$0.192^{0.075}_{0.058}$	$-0.17^{0.18}_{0.17}$		FS
33	Single Power Law	$0.085^{0.094}_{0.050}$	$-0.42^{0.39}_{0.42}$		FS
34	Single Power Law	$0.471^{0.406}_{0.218}$	$0.35^{0.35}_{0.32}$		PS

Notes. Column (1): source IDs. Column (2): model type that is used to fit the source radio spectral energy distribution. The single power law model has two free parameters: the reference flux and the spectral index. The piecewise power law is constructed from Equation 1 and has three free parameters: the turnover flux, the turnover frequency, and the spectral index below the turnover frequency. Column (3): best-fit reference fluxes (single-power-law-modeled sources) or turnover fluxes (piecewise-power-law-modeled sources), along with their 1σ uncertainties. For sources that are fit with a single power law, the reference flux is evaluated at 30 GHz. Column (4): best-fit spectral indices and 1σ uncertainties. For piecewise-power-law-modeled sources, these spectral indices are valid below the turnover frequency. Above the turnover frequency, the best-fit spectral index is -0.1. Column (5): best-fit turnover frequencies and 1σ uncertainties for all sources that are modeled with a piecewise power law. Column (6): Notes on individual sources. A 'PS' denotes a positive spectrum source with a best-fit spectral index between 0 and 2. An 'FS' denotes a flat spectrum source that is either a piecewise-power-law-modeled source, or a single-power-law modeled source with a best-fit spectral index that is consistent with -0.1 and between -1 and 0.5. An 'SS' denotes a steep spectrum source with a best-fit spectral index >2.

fit this model to the SEDs of all sources whose single power-law fits yield a reduced $\chi^2 > 2$. If the piecewise power law fit yields an improved reduced χ^2, then we use the piecewise power law to characterize the radio spectrum. Otherwise, we use the single power law model. The piecewise power law model has three free parameters: the turnover frequency, the turnover flux, and the spectral index below the turnover frequency. To ensure that our piecewise fits have one degree of freedom, we utilize the 5.25 and 7.5 GHz maps that are generated by imaging the two C-band basebands separately (see Section 3). We construct SEDs from flux measurements at 3.0, 5.25, 7.5, and 15.0 GHz, and fit the piecewise power law models to these SEDs.

Table 4 indicates which sources are characterized with a single or piecewise power law. For the sources that are characterized with a single power law, we show the best-fit spectral indices and reference fluxes in Table 4. For the sources that are characterized with a piecewise power law, we instead show the best-fit turnover frequencies, best-fit turnover fluxes, and best-fit spectral indices below the turnover frequency. Figure 11 shows the best-fit spectral indices and their uncertanties for all single-power-law-modeled sources. For the piecewise-power-law-modeled sources, we plot $\alpha = -0.1$, i.e., the best-fit spectral index above the turnover frequency. Finally, in the SED panels in Figures 4 - 9, we show the best-fit SEDs and 1σ confidence intervals that are derived from the single or piecewise power-law fits.

In general, the VLA-detected NGC 1977 sources have radio-SEDs that are consistent with free-free emission. Six sources—sources 9, 13, 15, 16, 27, and 31—prefer the piecewise power-law fit over the single power law fit and have best-fit turnover frequencies between $\sim$1 and 10 GHz. These sources are fit very well by the piecewise power-law model, suggesting that they are emitting free-free emission from a wind rather than a jet. Six of the single-power-law-modeled sources have relatively flat spectral indices that fall below the typical values measured towards jets ($\sim$0.5, Anglada et al. 2018), but overlap with the -0.1 value expected for optically thin free-free emission. These sources may be emitting optically thin free-free emission from a wind, although it is possible that their flat spectral indices are produced by a combination of optically thick free-free emission and non-thermal emission with a steep negative spectral index (see Section 4.3). Seven single-power-law-modeled sources have positive best-fit spectral indices that are above -0.1 and consistent with the typical values measured towards optically thick jets. Finally, one source, source 19, has a best-fit spectral index >2, which cannot be explained by optically thick free-free emission, but can be explained by dust emission (e.g., Hildebrand 1983).

In Tables 3 and 4, we label sources as flat spectrum (FS), positive spectrum (PS), or steep spectrum (SS) depending on the preferred model fit and the range of allowed spectral indices. The flat spectrum label is applied to all piecewise-power-law-modeled sources, and to all single-power-law-modeled sources with best-fit spectral indices that are consistent with optically thin free-free emission and between -1.0 and 0.5. Above 0.5, we expect values consistent with optically thick jets. Below -1.0, we expect values indicative of non-thermal emission dominating the continuum. The positive spectrum label is applied to all single-power-law-modeled sources with positive best-fit spectral indices between 0 and 2. Finally, the steep spectrum label is applied to source 19, the one single-power-law-modeled source with a best-fit spectral index >2. We do not label any sources whose range of allowed spectral indices overlaps with the above categories, since it is less clear whether they are emitting optically thin free-free emission, optically thick free-free emission, or emission from another mechanism.

4.3. *Circularly Polarized Emission*

Radio observations of ionized winds or outflows can in some cases be contaminated by non-thermal gyrosynchrotron emission produced from stellar magnetospheric activity (Dulk 1985). Gyrosynchrotron emission typically exhibits a steep negative spectral index at centimeter wavelengths, although for some electron energy distributions, the spectral index can be flatter and more similar to optically thin free-free emission (e.g., Güdel 2002). In this scenario, one of the main ways to discriminate between optically thin free-free emission and flat-sloped gyrosynchrotron emission is through measurements of circular polarization, computed as the ratio of the Stokes V (circularly polarized) and Stokes I (total intensity) flux densities (e.g., Feigelson et al. 1998; Zapata et al. 2004b). This is because optically thin gyrosynchrotron emission has moderate-to-high levels of circular polarization at radio wavelengths (>10%; Dulk 1985), whereas optically thin free-free emission does not.

Here we use measurements of circular polarization to examine whether the radio-SEDs of any of our detected NGC 1977 sources are contaminated with gyrosynchrotron emission. For each cluster member that we detect in the Stokes I plane, we search for circularly polarized emission in the Stokes V plane towards the same position as the detected Stokes I emission. If Stokes V emission is detected above 2.5σ (see Section 4.1), then we calculate the Stokes V flux density using the same aperture that was employed in the Stokes I

plane, and compute the circular polarization fraction as the ratio of the measured Stokes V and Stokes I fluxes. If no Stokes V emission is detected, then we calculate an upper limit on the circular polarization fraction using the measured Stokes I flux and the 2.5σ upper limit on the Stokes V flux.

In total, circularly polarized emission was detected towards only 4 of the 34 Stokes-I-detected NGC 1977 cluster members: sources 2, 22, 28, and 29. For sources 2, 22, and 28, the Stokes V emission is detected in the 6.4 GHz band only. For source 29, the detected Stokes V emission is in the 3.0 GHz band only. In all cases, the detecections are at marginal statistical significance ($2.5\sigma - 3.5\sigma$). Nevertheless, we find that the circular polarization fractions implied by the detected Stokes V emission are >10% by more than 1σ and, thus, consistent with the polarization fractions expected from gyrosynchrotron emission. The detected radio emission towards sources 2, 22, 28, and 29, may therefore be tracing gyrosynchrotron emission in addition to, or instead of, free-free emission. In Table 3, we labels sources 2, 22, 28, and 29 as likely gyrosynchrotron emitters based on their measured circular polarization fractions.

Because source 2 (proplyd KCFF2) has 6.4 GHz emission that is spatially separated from both central star and detected 3.0 GHz emission, it is possible that the 3.0 GHz emission is tracing free-free emission from the proplyd head (see Section 4.1.1), while some of the detected 6.4 GHz emission is tracing polarized emission from another component of the YSO, such as a non-thermal jet. Non-thermal jets are rarer than thermal jets, but a handful have been detected towards low-mass YSOs (e.g., Tychoniec et al. 2018a). These jets typically have a double-lobed morphology with peaked emission that is offset from the central protostar, similar to what is observed at 6.4 GHz towards source 2 (see Figure 10).

For sources 9, 15, and 16, no Stokes V emission is detected, but the upper limits imply circular polarization fractions of <10%. These limits are below the minimum circular polarization fraction expected for radio-wavelength gyrosynchrotron emission from an individual star, so the radio emission observed towards sources 9, 15, and 16 is unlikely to be contaminated with gyrosynchrotron emission. These 3 sources are bright in the Stokes I plane, detected in all three continuum bands, and have SEDs that are well reproduced by a piecewise power-law model (see Figures 4 - 9). In Table 3, we label sources 9, 15, and 16 as sources whose SEDs are not contaminated with gyrosynchrotron emission.

For the majority of NGC 1977 cluster members with non-detected Stokes V emission, the upper limits on the circular polarization fractions vary from $\lesssim$20% to $\lesssim$80%. These limits are not stringent enough to determine whether the radio-wavelength SEDs are contaminated with gyrosynchrotron emission. Deeper observations are needed to explicitly rule out the possibility of gyrosynchrotron contamination for these sources.

Finally, we note that the Stokes V detection rate is higher among the background radio sources that are detected in the Stokes I plane of our VLA maps (see Appendix A). Extragalactic objects are known to emit strong levels of gyrosynchtrotron emission (e.g., Condon 1992), and so we expect some background sources in our maps to be emitting circularly polarized radio emission.

4.4. *Variable Sources*

Here we search for evidence of variability among the subset of the NGC 1977 cluster members that are detected in both our VLA maps and in the previous VLA maps of Kounkel et al. (2014). For each of these sources, we compare our 6.4 GHz flux measurement with the average of the 4.5 and 7.5 GHz flux measurements from Kounkel et al. (2014), and then identify variable sources as the ones for which the 6.4 GHz flux measurement and average Kounkel et al. (2014) flux measurement differ by more than 3σ. Taking the average of the Kounkel et al. (2014) flux measurements allows us to obtain an approximate 6.4 GHz flux estimate at this earlier epoch. To ensure that none of the sources with intrinsically steep spectral indices are misidentified as variable as a result of comparing flux measurements at slightly different frequencies, we include a minimum variability percentage of 20% in our criteria for variable source identification. We define the variability percentage as the ratio of the standard deviation to the mean of our 6.4 GHz flux measurement and the average Kounkel et al. (2014) flux measurement.

With these criteria, we identify 6 cluster members as variable: sources 10, 22, 26, 27, 28, and 29. Of these 6 sources, 4 are spatially resolved (sources 10, 27, 28, and 29), and 3 are also detected in the Stokes V plane (sources 22, 28, and 29). In Table 3, we label sources 10, 22, 26, 27, 28, and 29 as variable.

Sources 22 and 26 show a particularly strong degree of radio variability. For these sources, our measured 6.4 GHz fluxes are more than 5 times lower than the previously reported fluxes from Kounkel et al. (2014). These levels of variability are stronger than the typical values measured towards thermal jets or winds (e.g., Anglada et al. 2018, and references therein), but they are consistent with the values expected from stellar gyrosynchrotron emission, which is known to be highly variably on short timescales (e.g., Feigelson & Montmerle 1985).

4.5. *Classification of NGC 1977 Radio Sources*

Following the discussion in Sections 4.1 - 4.4, we classify the radio-detected NGC cluster members into different categories based on the observed characteristics of the detected radio emission. In Table 3, we include a column that indicates all source classifications.

We first classify sources 1, 2, 3 (proplyds KCFF1, KCFF2, and KCFF3) as "Known Proplyds," since the detected radio emission of these sources is spatially coincident with the HST- or Spitzer-identified proplyd heads and spectrally consistent with optically thin free-free emission. For source 2, however, we note that the measured 6.4 GHz emission may be tracing a nonthermal jet in addition to the proplyd head.

We then classify additional radio-detected NGC 1977 cluster members as "Candidate Proplyds," "Candidate Jets," or "Radio Stars" based on their radio spectral indices, circular polarization, and/or radio variability. In principle, morphology would be the most effective characteristic for distinguishing between free-free emission from a wind, free-free emission from a jet, or gyrosynchrotron emission from a compact region of magnetic reconnection near the central star. However, most of our detections are unresolved, and the resolved detections exhibit radio morphologies that, at our current resolution, are consistent with the morphologies of both winds and jets. We therefore exclude morphology as a criterion when classifying radio detections without HST- or Spitzer-identified proplyds. We note, however, that some of the sources that we classify as "Candidate Proplyds" or "Candidate Jets" are marginally resolved, whereas none of the sources that we classify as "Radio Stars" are resolved (see Table 3).

We classify all flat spectrum (FS) sources with non-detected Stokes V emission as candidate proplyds, since the low (< 10 GHz) turnover frequencies and/or flat spectral indices of these sources are more likely to be explained by free-free emission from a wind than from a jet. As shown in Table 3, this selection criteria yields 10 candidate proplyds: sources 9, 13, 15, 16, 20, 21, 27, 31, 32, and 33. Three of these candidate proplyds have Stokes V upper limits that explicitly rule out potential contamination from gyrosynchrotron emission (sources 9, 15, 16). For the remaining candidate proplyds, deeper imaging, Stokes V observations, and/or time monitoring is needed to firmly rule out contributions from gyrosynchrotron emission.

We classify all positive spectrum (PS) sources (sources 5, 8, 12, 14, 23, 29, 34) as candidate jets, since these sources have positive radio spectral indices that are consistent with the free-free emission being optically thick, as expected for jets. For most jet candidates, the spectral indices are comparable to the typical values measured towards jets. For source 29, the spectral index is shallower than typical jet values, but the emission is circularly polarized (see Table 3), suggesting that gyrosynchrotron emission is contributing to the continuum and causing the overall spectral index to appear shallow. It is important to note that some of these jet candidates may be disk winds with free-free turnovers located just above the frequency range covered with our VLA observations (see Section 5.3). This can be tested with future observations at higher radio frequencies.

We classify sources 22 and 26 as radio stars since they exhibit a high level of variability that cannot be explained by free-free emission from a wind or jet but can be explained by gyrosynchrotron emission from stellar magnetic reconnection. Both of these sources are unresolved and detected in the 6.4 GHz band only, and source 22 is circularly polarized, further pointing to stellar gyrosynchrotron emission as the sole emission mechanism.

We classify source 19 as a protostar. The steep spectral index of source 19 suggests that its radio continuum is dominated entirely by thermal dust emission. Assuming optically thin dust with a constant opacity and constant dust temperature of 20 K (Beckwith et al. 1990), the measured 15.0 GHz continuum flux of source 19 would imply an unreasonably high disk mass. We note, however, that the measured flux is compatible with hotter, optically thick dust surrounding less evolved class 0/I protostars (e.g., Sheehan et al. 2022).

The remaining 11 radio-detected cluster members are labeled as a 'Possible Proplyd,' 'Possible Jet,' or 'Possible Radio Star', depending on the uncertainties on their derived spectral indices and on whether or not they are detected in the Stokes V plane. If a source is undetected in the Stokes V plane and has a best-fit spectral index that overlaps with our criteria for a flat or positive spectrum (see Section 4.2), we refer to it as a possible proplyd, since its spectrum is consistent with, albeit broadly, free-free emission. Alternatively, if a source has a best-fit spectral index that overlaps with our criteria for a positive or steep spectrum, we refer to it as a possible jet. The only exceptions to these two classification schemes are sources 24 and 28. We classify source 24 as a possible radio star, because its best-fit spectral index trends toward steep negative values suggestive of non-thermal emission (see Figure 11). And finally, we classify source 28 as a possible jet rather than a possible proplyd, since it is detected in the Stokes V plane and, thus, likely has a steeper-than-measured free-free spectral index. For all of these 11 sources, we emphasize that while we are somewhat able to narrow down their

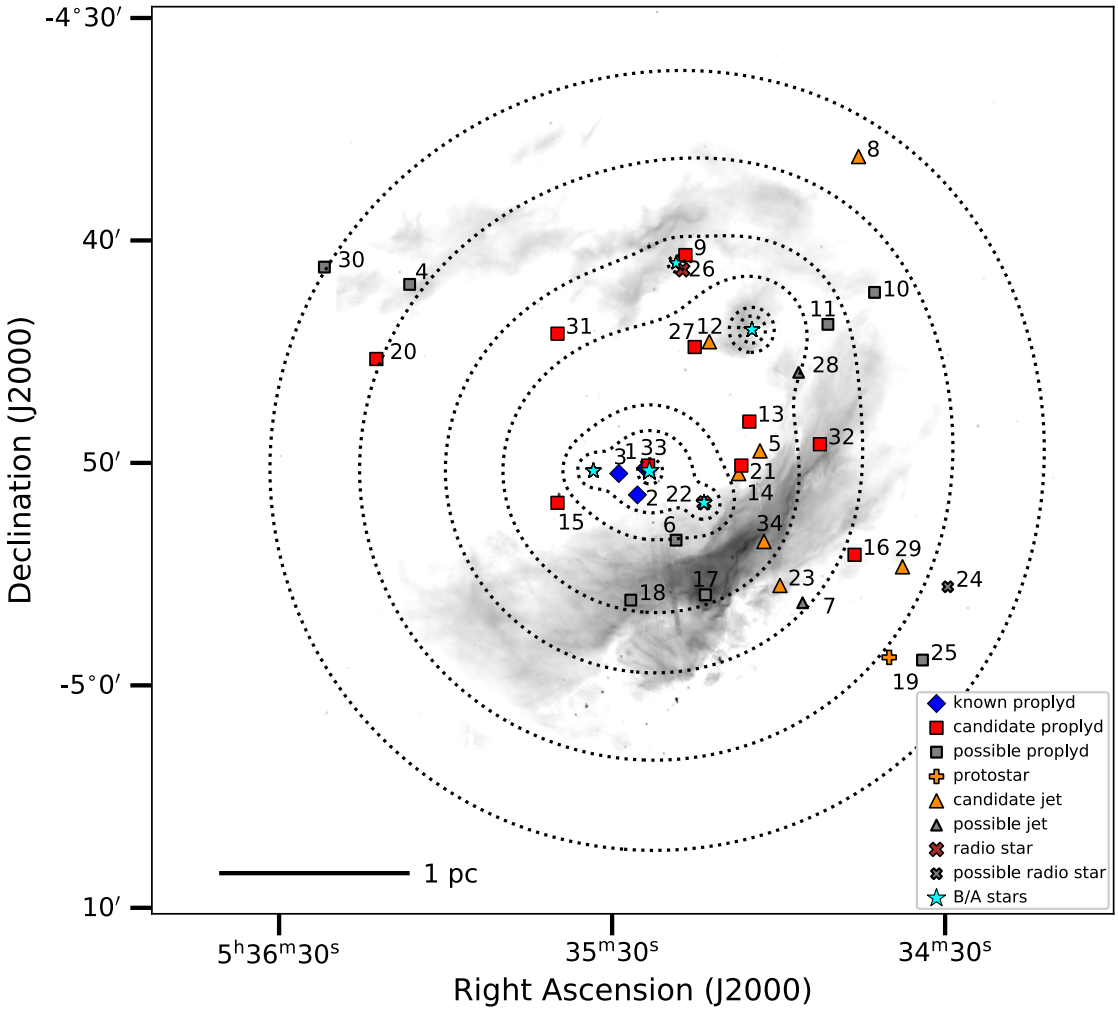

Figure 12. Spatial distribution of VLA-detected NGC 1977 cluster members. The layout of this plot is similar to that of Figure 1, except here we include dotted contours that show the local FUV radiation field strength at 15 G_0, 25 G_0, 50 G_0, 100 G_0, 500 G_0, 1000 G_0, and 10,000 G_0, where $G_0 = 1.6 \times 10^{-3}$ erg cm^{-2} s-1 (Habing 1968). Sources are color- and symbol-coded based on their radio classifications in Table 3. The source IDs are listed near the position of each source symbol.

nature, additional data is needed to determine they are winds, jets, or gyrosychrotron-dominated radio sources.

5. DISCUSSION

5.1. *Disk Photoevaporation in an Intermediately-irradiated Star-forming Region*

The detection of several-dozen NGC 1977 cluster members at radio wavelengths allows for one of the first systematic investigations of YSOs in an intermediately-irradiated star-forming environment. In Figure 12, we show the spatial distribution of the 34 radio-detected NGC 1977 sources, compared with the spatial distribution of B- or A- type stars in NGC 1977, namely, 42 Ori, HD 37058, HD 294264, HD 369658, and HC 294262. We also include contours that show the local external FUV radiation field strength in NGC 1977. Here, the external FUV field is calculated by estimating the FUV-continuum luminosity of each B- or A- type star using the stellar evolutionary models of Diaz-Miller et al. (1998), and then computing a localized FUV flux at all positions in our VLA maps. The spectral types for 42 Ori (∼B1V), HD 37058 (∼B3V), HD 294264 (∼B3V), HD 369658 (∼B3V), and HC 294262 (∼A0) are taken from the literature (Peterson & Megeath 2008, and references therein), and they imply FUV-continuum luminosities of $\sim 5 \times 10^{47}$ s^{-1} for 42 Ori , $\sim 2 \times 10^{46}$ s^{-1} for HD 37058, HD 294264, and HD 369658, and $\sim 3 \times 10^{44}$ s^{-1} for HD 294262. Altogether, the B- or A- type stars in NGC 1977 stars produce an external FUV field that ranges from $\sim 10^4$ G_0 towards the center of NGC 1977, to ~ 10 G_0 in the outskirts of NGC 1977.

The radio-detected NGC 1977 sources are distributed throughout the cluster and, thus, exposed to a range of intermediate FUV fields (between ∼10 and 10^4 G_0). The known proplyds that we detect are all located in the cluster center where the FUV field is $\sim 1,000 - 10,000$ G_0, as this was the region of NGC 1977 that was previously observed with HST (see Section 2). The newly-detected candidate proplyds tend to be located in regions where the FUV field is $\sim 50 - 1,000$ G_0, although we find one candidate proplyd in the inner $\sim 10,000$ G_0 region of NGC 1977, and another in the outskirts where the FUV field is ∼20 G_0. Half of jet candidates are positioned near one of more candidate proplyds, while the rest are located in the outskirts along with source 19, the candidate young protostar that we have identified. Finally, the two sources that we classify as radio stars are in very close proximity to a B- or A-type star. This, along with the close proximity of some jet candidates and proplyd candidates, demonstrates how both gyrosynchrotron-dominated radio sources and free-free-emitting jets can be located in the same regions of a cluster where expect to find populations of photoevaporating disks.

Numerical simulations widely predict that intermediate FUV fields are sufficient enough to launch photoevaporative winds that dominate over internally-driven mechanisms of disk dispersal and drive disk mass loss at rates $\gtrsim 10^{-8} - 10^{-6}$ $M_\odot$ yr^{-1} (e.g., Adams et al. 2004; Clarke 2007; Facchini et al. 2016; Haworth et al. 2018a,b; Haworth & Clarke 2019; Coleman & Haworth 2022). Recent ALMA surveys in Orion have also found indirect evidence of external photoevaporation in intermediate-UV environments, revealing that disks close to B- and A-type stars are on average $\sim 2 - 4$ times less massive than the disks further away from B- and A-type stars (van Terwisga et al. 2019; van Terwisga & Hacar 2023). Despite these findings, identifying direct signatures of external photoevaporation has proven challenging outside of the $> 10^4$ G_0 regions of the ONC and other O-star-hosting clusters, where many disks are exposed not only to intense FUV irradiation, but also to intense EUV irradiation that can externally ionize FUV-driven photoevaporative winds to point where large samples of ionized winds become bright and easy to see with the VLA (e.g., Churchwell et al. 1987; Garay et al. 1987; Felli et al. 1993a,b; Forbrich et al. 2016; Sheehan et al. 2016), HST (e.g., O'dell & Wen 1994; Bally et al. 1998, 2000; Ricci et al. 2008; Smith et al. 2010; Fang et al. 2012; Haworth et al. 2021), VLT-MUSE (e.g., Haworth et al. 2023; Aru et al. 2024), JWST (Berné et al. 2022; Habart et al. 2023; McCaughrean & Pearson 2023), and ALMA (Ballering et al. 2023).

If the newly-detected candidate proplyds in our sample are indeed YSOs with externally-evaporating disks, as suggested by their free-free emission spectra and, in several cases, their lack of circular polarization and/or radio variability, this would demonstrate the use of broadband radio photometry for identifying externally-evaporating disks in intermediatly irradiated regions of star formation. Higher-resolution imaging of the NGC 1977 region—with the VLA, ALMA, HST, VLT-MUSE, and/or JWST—is needed to spatially resolve free-free emission structures, confirm the disk-wind nature of our photometrically-identified candidate proplyds, and explicitly rule out the possibility of gyrosynchrotron contamination for the majority of Stokes-V-nondetected candidate proplyds. Deeper imaging can also improve uncertainties in the flux measurements and hence the inferred radio spectral indices of all VLA-detected sources in our maps, including possible proplyds, possible jets, and background extragalactic objects.

5.2. *Mass-loss rates*

Measuring the mass-loss rates of protoplanetary disks provides crucial tests for understanding the impact of the stellar cluster environment on disk properties and evolution. Here we measure the mass-loss rates of our VLA-detected proplyds and candidate proplyds by computing the steady-state mass flow through a sphere at the location where the ionized wind is launched, via $\dot{M} = 4\pi r^2 \rho v$. We assume a fully ionized flow, such that the gas density can be expressed in terms of the electron density, n_e, as $\rho = \mu m_H n_e$, where $\mu = 1.35$ is the mean molecular weight of the ionized gas and m_H is the mass of a hydrogen atom. For the outflow velocity, we adopt $v = 10$ km s^{-1} (typical for ionized photoevaporative winds; e.g., Johnstone et al. 1998).

Since most of our VLA detections are unresolved or marginally resolved, we are unable to spatially isolate the wind launching radius with our VLA observations. Sources 2 and 3, however, have proplyd ionization fronts that are well-resolved with HST (see Figure 10). Since these ionization fronts mark the approximate location where the photovaporative winds become fully ionized, we calculate $\dot{M}$ for sources 2 and 3 at the location of the HST-identified ionization fronts, using the ionization front radii derived by Kim et al. (2016). For the remaining sources, we calculate $\dot{M}$ assuming an upper limit to the wind launching radius. We approximate the launching radius as the half-width-at-half maximum of the synthesized beam major axis, using the beam size from the highest frequency observations at which the detected free-free emission is consistent with being optically thin. As shown in Table 1, this typically results

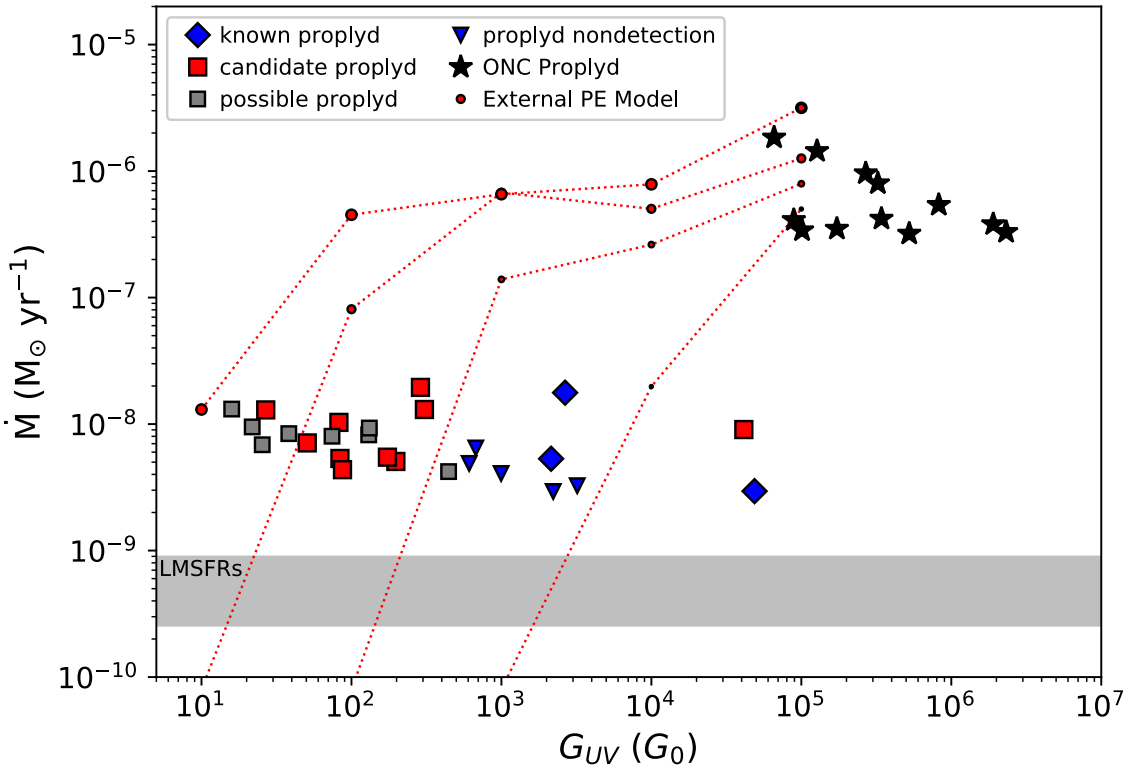

Figure 13. Photoevaporative mass loss rates ($\dot{M}$) derived from Equation 3 for all known, candidate, and possible NGC 1977 proplyds detected in our VLA maps, plotted as a function of the local FUV radiation field strength. We also include points showing the mass-loss rates inferred from the 4σ 6.4 GHz upper flux limits that are measured towards the VLA–non-detected known proplyds from Bally et al. (2012) and Kim et al. (2016). We also show the mass loss rates derived by Ballering et al. (2023) for a subset of ALMA-detected proplyds in the ONC, where the FUV radiation field strength towards the ONC proplyds is calculated using a FUV photon luminositiy of 7.0×10^{48} s^{-1} for θ^1 Ori C (Johnstone et al. 1998; Störzer & Hollenbach 1999; O'Dell et al. 2017), which we assume as the sole, dominant source of external FUV radiation in our calculations. The shaded grey region indicates the 1σ region around the median internally-driven wind mass-loss rates derived by Fang et al. (2018) towards a sample of disks in low-mass star-forming regions (LMSFRs). The dotted red lines show predicted mass loss rates (as a function of the FUV field strength) from the `FRIED` grid of externally evaporating disk models (Haworth et al. 2018b), with the different lines corresponding to models with different disk radii. The model disk size is directly proportional to the marker size of the plotted red circles, and we show the predicted mass loss rates for disk radii of 20 AU (smallest circles), 40 AU, 75 AU, and 150 AU (largest circles). All plotted models share a common initial disk mass of ~ 5 Jupiter masses, and a common central stellar mass of ~ 0.5 M$_\odot$.

in $r \sim 0\farcs5 - 1''$ ($\sim$200 – 500 AU), i.e., values that are similar to the ionization front radii of proplyds in the ONC (e.g., Ballering et al. 2023).

For an optically thin ionized wind, the electron density can be derived from the emission measure, $EM \approx n_e^2 L$, where L is line-of-sight path length through the emitting region. We calculate the emission measure using Equation A.1b of Mezger & Henderson (1967):

$$\left(\frac{EM}{\text{pc cm}^{-6}}\right) = \left(\frac{\tau_{ff}}{3.28 \times 10^{-7}}\right)\left(\frac{T_e}{10^4 \text{ K}}\right)\left(\frac{\nu}{\text{GHz}}\right), \quad (2)$$

where τ_{ff} denotes the line-of-sight optical depth of the ionized gas, and T_e denotes the electron gas temperature (Mezger & Henderson 1967). Again, we compute τ_{ff} at the highest frequency at which the detected free-free emission is optically thin via $\tau_{ff} = I_\nu / B_\nu(T_e)$, where I_ν is the measured peak surface brightness of the free-free emission, and $B_\nu(T_e)$ is the Planck function. For an electron temperature of 10^4 K, we obtain emission measures in the range $\sim 10^3 - 10^5$ pc cm^{-6} for our VLA-detected sources.

Previous studies of the ONC proplyds have computed the line-of-sight path length assuming that the ionized winds have a hemispherical geometry or a thin spherical shell geometry (e.g., Bally et al. 1998; Ballering et al. 2023). We compute the line-of-sight path length through our NGC 1977 proplyds and candidate proplyds using the same thin shell geometry assumed by Ballering et al. (2023), in which case the path length is approximated as $L = 2\sqrt{2r/n_e\sigma}$, where $\sigma = 6.3 \times 10^{-18}$ cm^2 is the

ionization cross section. This choice allows for a direct comparison of the photoevaporative mass-loss rates derived from measurements of free-free emission in NGC 1977 vs. the ONC. If any our NGC 1977 sources have more spatially extended distributions of ionized gas, as expected for an isotropic or internal ionization source (see Section 5.4), we would expect the inferred electron densities and, thus, mass loss rates to be, at most, an order of magnitude lower as a result of the increased path length. For example, if were to assume a uniform sphere of ionized gas (i.e., $L \approx 2r$), the electron densities would be $\sim 3-4$ times lower than the values inferred under the hemispherical shell geometry.

With our choice of path length geometry, the mass-loss rate can be expressed in terms of the flow velocity, launching radius, and emission measure (i.e., free-free emission surface brightness) as

$$\dot{M} = 2\pi\mu m_H v \sigma^{1/3} E M^{2/3} r^{5/3}. \quad (3)$$

This equation is valid over frequencies where the ionized winds are optically thin. In the optically thick regime, the mass-loss rates can also be derived from the mass-flow equation provided that the free-free fluxes, turnover frequencies, spectral indices, source distances, and source geometries are constrained (e.g., Panagia & Felli 1975; Reynolds 1986). Assuming a spherical wind geometry, we find that for the NGC 1977 sources that are fitted with a piecewise power law model and have evidence for a free-free turnover, the mass-loss rates derived in the optically thick regime are lower than, but within a order of magnitude of, the values derived in the optically thin regime via Equation 3.

Figure 13 shows the mass-loss rates obtained from Equation 3 for all VLA-detected proplyds and candidate proplyds in NGC 1977 as a function of the local FUV radiation field strength. We also include points showing the inferred mass-loss rates for possible NGC 1977 proplyds in our maps, and for all non-detected proplyds assuming an upper flux limit of 4σ and an ionization front radius from the literature. Finally, we include points showing the mass-loss rates derived by Ballering et al. (2023) for the subset of ALMA-detected ONC proplyds. Typically, we derive mass-loss rates of $\sim 10^{-9} - 10^{-8}$ $M_\odot$ yr^{-1} for the NGC 1977 sources, although in most cases, the derived mass-loss rates may be upper limits due to the values we have assumed for the wind launching radii and/or line-of-sight path-lengths. Overall, the mass-loss rates of our NGC 1977 sources are significantly lower than the mass loss rates of the ALMA-detected ONC proplyds, by up to two orders of magnitude. If any of our newly-identified candidate proplyds have smaller wind launching radii than the values assumed in our calculations—as expected for an internally-driven photoevaporative wind (see Section 5.3)—then the derived mass-loss rates would be even lower.

The lower mass-loss rates derived towards our NGC 1977 sources suggest that disks in NGC 1977 may be less prone to the "proplyd lifetime problem" than disks in the ONC. The lifetimes of disks in clustered star-forming regions can be estimated by dividing the total mass of a photoevaporating disk by the derived photoevaporative mass-loss rate, and in the ONC, these calculations typically result in lifetimes of $\sim 1-100$ kyr, which are orders of magnitude lower than the $\sim$1 Myr age of the ONC (for recent mass loss estimates, see Ballering et al. 2023). The mismatch in the derived lifetimes vs. stellar ages suggest that disk-proplyd systems in the ONC should have dispersed well before the present time in which they are being observed, unless they are more massive than typically assumed (e.g., Clarke 2007), and/or have more recently begun to photoevaporate due to extinction effects, dynamical effects, or younger-than-assumed stellar ages (e.g., Scally & Clarke 2001; Winter et al. 2019; Qiao et al. 2022). If we assume that the VLA-detected NGC 1977 sources have similar disk masses as the ONC proplyds, then the derived lifetimes would be $\sim 0.1-10$ Myr, which are longer than the derived lifetimes of ONC proplyds, and consistent with the $\sim$1 Myr age of NGC 1977 (e.g., Da Rio et al. 2016).

5.3. *Evidence for spatially-extended externally-evaporating disks in NGC 1977*

Although we find lower photoevaporative mass-loss rates in NGC 1977 than in the ONC (see Figure 13), the derived mass-loss rates are consistent with the values predicted by models of external photoevaporation in intermediate-UV environments. In Figure 13, we include red dashed lines that show the predicted mass-loss rates of externally evaporating disks with different disk sizes. The predicted mass-loss rates are taken from the `FRIED` grid of photoevaporating disk models (Haworth et al. 2018b), and we plot the mass-loss rates of models with an initial disk mass of $\sim$5 Jupiter masses, a stellar mass of 0.5 $M_\odot$, and a disk radius of either 20, 40, 75, or 150 AU.

For the candidate proplyds located at $\sim 20-500$ G_0, the derived mass-loss rates match up well with the predicted values of extended photoevaporating disk models with radii between $\sim$ 50 and 150 AU. For the two VLA-detected proplyds at $\sim$1000 G_0 (Sources 1 and 2, i.e., KCFF2 and KCFF3), we find that smaller evaporating disk models, with radii $\sim 20-40$ AU, are needed to produce an agreement between the inferred and predicted mass-loss rates. Finally, the candidate proplyd and

known proplyd at $\sim$10,000 G_0 (Source 33 and Source 3, i.e., KCFF 1) appear to have mass-loss rates that are lower than the values predicted by external photevaporation models. This discrepancy can be reconciled if the two sources are exposed to weaker FUV fields than what is implied by their projected separations from nearby B and A stars, due to projection or extinction effects (e.g., Winter et al. 2019; Parker et al. 2021a; Qiao et al. 2022). It can also be reconciled if the two sources have higher stellar masses than the 0.5 $M_\odot$ model values plotted in Figure 13, which seems plausible given the positions of cluster members on our near-infrared color-magnitude diagram (see Figure 2).

The model comparisons shown in Figure 13 suggest that NGC 1977 may contain a population of extended disks with systematically larger disk sizes than the compact disks typically found in the ONC (e.g., Eisner et al. 2018; Boyden & Eisner 2020; Otter et al. 2021). In the harsh $>10^5$ G_0 regions of the ONC, the external FUV field is strong enough such that even compact ($R = 20-30$ AU) disks are expected to undergo intense external photoevaporation and truncate down to smaller disk sizes (e.g., $R \lesssim 5$ AU) before no longer being subject to significant mass loss (Haworth et al. 2018b, see Figure 13). In the more intermediately-irradiated environment of NGC 1977, however, only extended disks can experience significant mass loss (i.e., $\dot{M} > 10^{-10}$ $M_\odot$ yr^{-1}) from external photoevaporation, with $\gtrsim$50 AU radii required at 100 G_0, and $\gtrsim$100 AU radii required at 10 G_0. Our VLA-detected candidate proplyds at $\sim 10-1,000$ G_0 may therefore host spatially extended photoevaporating disks with sizes that are similar to the values commonly found in lower-mass star-forming regions (e.g., Ansdell et al. 2018; Sanchis et al. 2021). The VLA-detected proplyds and candidate proplyds at $\sim 1000-10,000$ G_0, however, appear likely to host compact disks with comparable sizes as the ONC proplyds (see Figure 13).

While FUV-driven winds due to external photoevaporation are expected to dominate the mass evolution of the outer regions of protoplanetary disks in intermediate-UV environments, we can also examine whether some of the observed free-free fluxes in NGC 1977 are produced by strong, internally-generated disk winds. The inner regions of protoplanetary disks are thought to launch magnetohydrodynamic (MHD) and photoevaporative winds that can also deplete disks of planet-forming material, where these winds are driven by internal magneto-centrifugal processes and ionizing photons from the central star, respectively (for a recent review of inner disk winds, see Pascucci et al. 2022). Surveys of disk forbidden line emission typically derive mass-loss rates of around $\sim 10^{-9}$ $M_\odot$ yr^{-1} for internally-generated disk winds (e.g., Natta et al. 2014; Fang et al. 2018), which are somewhat lower than the inferred mass loss rates of our NGC 1977 sources (see Figure 13). Some class II objects, however, are found to have higher wind mass-loss rates of $\gtrsim 10^{-8}$ $M_\odot$ yr^{-1}, where these sources typically have high accretion rates (e.g., Fang et al. 2018), and are theorized to be X-ray active (e.g., Owen et al. 2012; Picogna et al. 2019; Ercolano et al. 2021).

If our VLA-detected sources in NGC 1977 are biased towards high accretion rates or high X-ray luminosities, then we might expect some of the derived mass-loss rates to be consistent with a strong internal disk wind. However, this scenario seems unlikely to apply to the candidate proplyds with evidence for a free-free turnover (see Table 4). The free-free emission spectrum of a vigorous X–ray-driven disk wind (i.e., $\dot{M} > 10^{-9}$ $M_\odot$ yr^{-1}) is predicted to have a relatively high turnover frequency (>20 GHz) as a result of intense X–ray-driven heating and ionization of bound material close (<1 AU) to the central star (e.g., Owen et al. 2013). Six of our photometrically-identified candidate proplyds have turnover frequencies between 1 and 10 GHz (see Table 4), suggesting that they are not irradiated by enough X-ray photons to launch a strong inner disk wind that is optically thick over the full radio spectrum.

Spatially resolved imaging of the central disks and surrounding winds, combined with constraints on the free-free turnover frequency, could help identify which cluster members in NGC 1977 are launching internally- versus externally-driven disk winds. If any of the VLA-detected sources in our sample have compact disk sizes that are smaller than the values consistent with external photoevaporation models, then these would be more likely to be launching internally, rather than externally, driven disk winds.

5.4. *Proplyd Illumination Sources in NGC 1977*

Here we examine which ionization sources in NGC 1977 are responsible for ionizing and, thus, illuminating our radio-detected proplyds and candidate proplyds. Measurements of optically thin free-free emission relate directly to an ionizing photon flux via the "Volume Emission Measure," defined as:

$$\frac{VEM}{\mathrm{cm}^{-3}} = 2.9\times10^{50}\left(\frac{S_\nu}{\mathrm{mJy}}\right)\left(\frac{\nu}{\mathrm{GHz}}\right)^{0.1}\left(\frac{T_e}{10^4\mathrm{K}}\right)^{0.35}\left(\frac{d}{\mathrm{pc}}\right)^2, \quad (4)$$

where S_ν is the measured flux of the free-free emission, ν is the frequency at which the free-free emission flux is measured, T_e is the electron temperature of the ionized gas, and d is the source distance (Mezger & Henderson

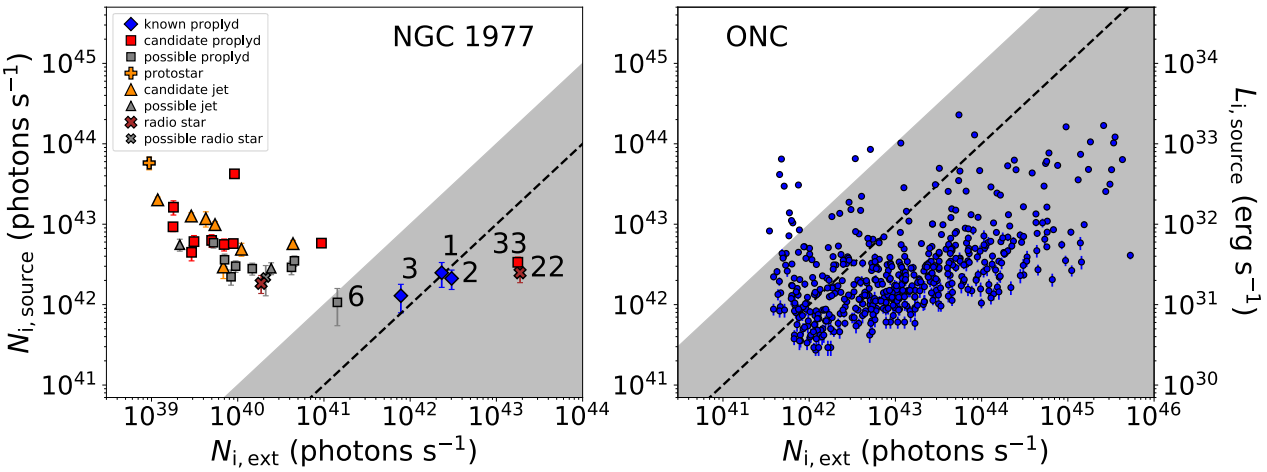

Figure 14. Ionizing photon rates ($N_{\rm i,source}$) derived from Equation 5 for all for all NGC 1977 cluster members detected in our VLA maps (left panel), and all compact radio sources in the central $20' \times 20'$ region of the ONC (right panel). The ionizing photon rates are plotted as a function of the local rate of ionizing EUV photons ($N_{\rm i,ext}$) provided by massive stars in each region. The ionizing photon rates are shown in both units of photons s^{-1} and in units of erg s^{-1}, where the conversion factor from photon s^{-1} to erg s^{-1} is $\sim 2.2 \times 10^{-11}$. The dashed black line indicates where $N_{\rm i,source} = N_{\rm i,ext}$, while the shaded gray region depicts where $N_{\rm i,source} \leq 10 \times N_{\rm i,ext}$. NGC 1977 sources within the shaded gray region are indicated with their source IDs listed in Table 3. To derive ionizing photon rates for the ONC sources, we use the 6.0 GHz continuum flux measurements from Vargas-González et al. (2021).

1967). The rate of ionizing photons required to ionize the gas is $N_i = \alpha VEM$, where α is the recombination coefficient. Assuming $\alpha = 2.6 \times 10^{-13} (T_e/10^4{\rm K})^{-0.8}$ (e.g., Churchwell et al. 1987; Garay et al. 1987), $T_e = 10^4$ K, and $d = 400$ pc, N_i can be written in terms of the free-free flux as:

$$\frac{N_i}{\rm s^{-1}} = 1.2 \times 10^{43} \left(\frac{S_\nu}{\rm mJy}\right) \left(\frac{\nu}{\rm GHz}\right)^{0.1}. \quad (5)$$

We use this equation to determine the ionizing photon rates that are required to produce the observed free-free fluxes of known proplyds and new candidate proplyds in NGC 1977. We also use this equation to compute the ionizing photon rates implied by the measured fluxes of other radio-detected cluster members, including jet candidates, possible proplyds or jets that are potentially emitting free-free emission, and gyrosynchrotron- or dust-dominated radio sources. For the sources where we clearly identify the optically thick and thin components of the free-free emission spectrum, we compute the ionizing photon rate at the highest frequency in which the free-free emission is detected and consistent with being optically thin. For all other sources, we use the measured radio fluxes at the highest detected frequency to compute the ionizing photon rate.

Figure 14 shows the rate of ionizing photons derived from Equation 5 as a function of the local rate of incident ionizing photons from known B- and A- type stars in NGC 1977, i.e., 42 Ori, HD 37058, HD 294264, HD 369658, and HD 294262. For each B- or A-type star, we compute an ionizing photon rate incident on an NGC 1977 radio source using the EUV-continuum luminosities from the evolutionary models of Diaz-Miller et al. (1998) and the same source sizes used to derive the photoevaporative mass-loss rates (see Section 5.2). We then sum the individual external ionizing photon rates provided by each B or A star to obtain a total external ionizing photon rate. We assume no intracluster extinction in these calculations, and use an EUV-continuum luminosity of 10^{46} s^{-1} for 42 Ori, an EUV-continuum luminosity of 10^{43} s^{-1} for HD 37058, HD 294264, and HD 369658, and an EUV-continuum luminosity of 10^{37} s^{-1} for HD 294262.

We also include a panel in Figure 14 that shows the number of ionizing photons derived for compact radio sources in the ONC, in order to compare the number ionizing photons derived for sources in NGC 1977 vs. the ONC. Radio continuum flux measurements for the ONC sources are taken from Vargas-González et al. (2021), who compiled 6.0 GHz continuum flux measurements for a sample of $\sim$500 sources within the central $20' \times 20'$ region of the ONC. To calculate the number of EUV photons provided by massive stars in the ONC, we assume that θ^1 Ori C is the sole, dominant producer of external EUV radiation, and we adopt an EUV-continuum luminosity of 7×10^{48} erg s^{-1} (Johnstone et al. 1998; Störzer & Hollenbach 1999; O'Dell et al. 2017).

Figure 14 suggests that B- and A-type stars in NGC 1977 do not produce enough EUV radiation to externally ionize and externally illuminate most of the radio-

detected NGC 1977 sources in our VLA maps. In order for a free-free emitting source to be illuminated by external ionizing radiation, the number of ionizing photons derived from Equation 5 must be less than or equal to the localized number of ionizing photons provided by massive stars, as found towards proplyds and YSOs in the core of the ONC (e.g., Churchwell et al. 1987; Garay et al. 1987; Zapata et al. 2004a,b; Forbrich et al. 2016; Sheehan et al. 2016; Vargas-González et al. 2021; Ballering et al. 2023, see also Figure 14). Of the 34 radio-detected NGC 1977 sources plotted in Figure 14, only 4 satisfy this requirement: sources 1, 2, 22, and 33. If the EUV-continuum luminosities of NGC 1977's B and A stars were $\sim 2-10$ times more luminous than assumed, then 2 additional sources would satisfy this requirement: sources 3 and 6. As shown in Figure 12, sources 1, 2, 3, 6, 22, and 33 are all located in the core of NGC 1977 near 42 Ori, with sources 1, 2, and 3 being known proplyds, source 33 being a newly-identified candidate proplyd, source 6 being a possible proplyd, and source 22 being a radio star that is likely emitting gyrosynchrotron emission rather than free-free emission.

The free-free emission that we measure towards sources 1, 2, and 33 can therefore be produced by gas that is externally ionized by EUV radiation from 42 Ori, with additional contributions from HD 37058, HD 294264, HD 369658, and HD 294262. If we have underestimated the EUV luminosities of 42 Ori, HD 37058, HD 294264, HD 369658, and/or HD 294262, then we might also expect the radio emission from source 3 and, if emitting free-free emission, source 6 to be produced by gas that is externally ionized by neighboring B- or A-type stars. For all other free-free emitting NGC 1977 radio sources in our sample, including any possible proplyds that are potentially emitting free-free emission, other ionization sources are needed to produce the $\gtrsim$0.1 mJy radio fluxes that we are measuring.

Unless a photoevaporating disk is located in the core of NGC 1977, we might expect its wind to be illuminated by internal ionizing radiation from the central star (e.g., Pascucci et al. 2012; Owen et al. 2013; Pascucci et al. 2014), regardless of whether the wind is internally or externally driven. In Figure 14, we include an additional y-axis that shows the ionizing luminosities implied by the ionizing photon rates derived from Equation 5. These luminosities are consistent with the expected ionizing luminosities of pre-main-sequence stars (e.g., Alexander et al. 2005; Getman et al. 2005; Herczeg et al. 2007; Shkolnik & Barman 2014; Hartmann et al. 2016), although they tend to be on the more luminous end of expected values. The detection of radio emission towards a relatively small number of UV-luminous stars, however, matches up well with the overall low detection rates that we observe towards known YSOs in NGC 1977 (see Figure 3).

Given the potential prevalence of internally illuminated disk winds in NGC 1977, it is worth pointing out that externally driven but internally illuminated disk winds can have similar morphologies as externally driven and externally illuminated winds. The d203-506 disk in the Orion Bar, for example, is irradiated by a $\sim 10^4$ G_0 FUV field but shielded from the external EUV field (e.g., Champion et al. 2017), and recent infrared- and submillimeter-wavelength imaging of this disk has revealed that the photoevaporative wind surrounding d203-506 has the same cometary shape as the externally illuminated ONC proplyds (e.g., Haworth et al. 2023; Berné et al. 2024). This new imaging demonstrates that anisotropic FUV radiation fields play a dominant role in sculpting cometary wind morphologies when an external EUV radiation field is not present. Proplyd-like structures in NGC 1977 may therefore be expected outside of the more intensely EUV-irradiated cluster center, although in these regions the externally FUV-driven winds may have more uniform distributions of ionized gas, rather than distributions that are concentrated in a thin shell near an ionization front (see Section 5.2).

A deeper, higher-resolution VLA survey in NGC 1977 is needed to establish a larger sample of free-free emitting YSOs, rule out the possibility of gyrosychrotron contamination, and test whether most free-free-emitting sources in NGC 1977 are illuminated by internally or externally sourced radiation. If deeper observations were to reveal diffuse ionized wind structures whose free-free fluxes correlate with stellar UV or X-ray luminosity, this would point to internal ionization as the main illuminating source for ionized winds in NGC 1977, in which case some of the FUV-driven photoevaporative winds in NGC 1977 may only be partially ionized (e.g., Haworth & Clarke 2019). We note, however, that in order to enable investigations with stellar properties, additional spectroscopic data at other wavelengths are needed, as the majority of YSOs in NGC 1977 do not have published accretion rates or X-ray luminosities. If such measurements were obtained, and if deeper imaging were to instead reveal that most externally FUV-driven disk winds in NGC 1977 are surrounded by thin shells of ionized gas with brighter free-free fluxes than expected from internal illumination, this would point to other ionization sources as the dominant illumination mechanism and suggest that we are underestimating the amount of external ionization in NGC 1977.

Shock ionization has been proposed as an explanation for some of the bright ionization fronts observed

towards intermediately irradiated disks in the outskirts of the ONC, where the EUV field is low and the FUV field is $\sim$1000 G_0 (e.g., O'Dell & Beckwith 1997; Smith et al. 2005), and towards a subset of the more intensely irradiated ONC disks near the cluster center (e.g., Bally et al. 1998). Candidate proplyds in NGC 1977 may be externally illuminated by a similar mechanism if they are located near dense interstellar gas or high-mass stellar outflows. On the other hand, Figure 14 suggests that at least one known proplyd in NGC 1977 has a higher free-free flux than what is implied by the expected EUV luminosities of neighboring B and A stars. A similar inconsistency has been found by Bally et al. (2012) towards the NGC 1977 proplyd Parengo 2042, but with HST-based measurements of electron density. The EUV radiation field in NGC 1977 is therefore likely to be stronger than currently predicted, although it remains unclear whether this is due to an incorrect spectral type for one of the region's massive stars, or to a systematic underprediction of the EUV luminosities of young B-type stars, as has been observed towards the handful of evolved B stars where direct measurements of the ionizing UV flux are possible (e.g., Cassinelli et al. 1995).

6. CONCLUSIONS

We presented deep, multi-wavelength VLA observations covering the central $\sim 30' \times 45'$ region of NGC 1977 at 3.0 GHz, 6.4 GHz, and 15.0 GHz. We searched for compact radio sources in these maps using blind and catalog-driven approaches, and identified 56 sources at 3.0 GHz, 65 sources at 6.4 GHz, and 26 sources at 15.0 GHz, for a total 71 unique sources. Of these 71 VLA-detected sources, 3 are associated with HST- and/or *Spitzer*-identified proplyds in NGC 1977, 22 are associated with other YSOs in NGC 1977, 9 are newly-identified candidate members of NGC 1977, and 37 are background extragalactic objects that are not associated with NGC 1977. Thus, we detected a total of 34 confirmed or candidate NGC 1977 cluster members at centimeter wavelengths.

For each cluster member that we detected in our maps, we measured its flux density at 3.0, 6.4, and 15.0 GHz, computed the radio spectral index via single or piecewise power-law fits, and searched for signatures of circular polarization and/or radio variability. We then used the observed spectral, polarization, and temporal characteristics of the detected radio emission to identify candidate proplyds, candidate jets, and gyrosynchrotron-dominated radio sources.

We identify 10 new candidate proplyds in NGC 1977, effectively doubling the total number of candidate proplyds found in the region. Our newly-identified candidate proplyds have radio spectral energy distributions that are well-characterized by power-law free-free emission models with low turnover frequencies and/or flat spectral indices, as expected for ionized, externally evaporating disk winds. 9 of them are located in regions of NGC 1977 where the external FUV radiation field is $\sim 10 - 1000$ G_0, while one is located in the same >1000 G_0 region as the proplyds previously identified with HST and/or Spitzer imaging. High angular resolution observations are needed to confirm the disk-wind nature of our photometrically identified candidate proplyds. If confirmed, this would demonstrate the ability of broadband radio photometry to identify bright, externally evaporating disks in intermediately irradiated regions of star formation.

We have also used measurements of centimeter-wavelength free-free emission to calculate the mass-loss rates of known proplyds and newly-identified candidate proplyds in NGC 1977. The derived mass loss rates are $1 - 2$ orders of magnitude lower than the values obtained for proplyds in the central region of the ONC, suggesting that disks in NGC 1977 have longer lifetimes than disk-proplyd systems in the ONC. If the photoevaporative winds are internally driven, which we argued is possible for a subset of the VLA-detected cluster members, then the mass loss rates derived here would be upper limits. Our current VLA-derived mass-loss rates in NGC 1977 are consistent with the values predicted for spatially extended externally-evaporating disks that are irradiated by intermediate FUV fields. The intermediately-irradiated NGC 1977 cluster may therefore host a population of extended photoevaporating disks that are larger than the disks typically found in the ONC. Spatially resolved observations of the central disks and surrounding winds, however, are needed to test this hypothesis and to help identify any compact disks in NGC 1977 that are more likely to be launching internally, rather than externally, driven winds.

Finally, we computed the ionizing photon rates required to produce the measured free-free emission of our VLA-detected proplyds and candidate proplyds. We find that most of the candidate proplyds in NGC 1977, including one HST-identified proplyd, have free-free fluxes that are higher than the values implied by photoionizing radiation from neighboring B- and A-type stars. This marks a difference from photoevaporating disks in the core of the ONC, the majority of which are externally ionized by EUV radiation from the O star θ^1 Ori C. Photoevaporative disk winds in NGC 1977 may be illuminated by ionizing radiation from their central stars or by other sources of external ionization, unless

they are located very close to known B- and A-type stars in the region. The external EUV radiation field in NGC 1977 may also be larger than currently assumed, as suggested by this study and by previous studies in the region, although the exact degree of underestimation remains uncertain.

Our findings suggest that intermediately-irradiated regions of star formation host a less hostile environment for disk evolution and planet formation than the intensely-irradiated, proplyd hosting regions of the ONC and other O-star-hosting clusters. Disks in the ONC are severely truncated and photoevaporated by strong external UV fields, whereas disks in NGC 1977 appear likely to remain intact and long-lived despite ongoing external photoevaporation. The VLA-detected NGC 1977 sources presented in this study represent an ideal set of targets for future follow-up studies of disk demographics in intermediate-UV environments. Such environments represent the typical conditions of star and planet formation in the Galaxy.

Acknowledgements: We are grateful to P. Sheehan, who provided useful ideas for the initial development of this work. We also thank NRAO staff, especially Amy Kimball and Drew Medlin, for assistance with VLA scheduling blocks and Stokes V imaging. We also acknowledge the use of NRAO computing facilities for the reduction and imaging of the VLA data. Finally, we thank the anonymous referee, whose feedback improved the clarity and organization of this manuscript. This work was supported by NSF AAG grant 1811290, and by NRAO Student Observing Support Award SOPS21A-001. R. Boyden also acknowledges support from the University of Arizona's Marshall Foundation Dissertation Fellowship, the Virginia Initiative on Cosmic Origins (VICO), and NSF grant no. AST-2206437. The National Radio Astronomy Observatory is a facility of the National Science Foundation operated under cooperative agreement by Associated Universities, Inc. Some of the data presented in this paper were obtained from the Mikulski Archive for Space Telescopes (MAST) at the Space Telescope Science Institute. The specific observations analyzed can be accessed via 10.17909/bagj-yf51. This material is based upon work supported by the National Aeronautics and Space Administration under Agreement No. 80NSSC21K0593 for the program "Alien Earths." The results reported herein benefitted from collaborations and/or information exchange within NASA's Nexus for Exoplanet System Science (NExSS) research coordination network sponsored by NASA's Science Mission Directorate.

Facility: NSF's Karl G. Jansky Very Large Array (VLA)

Software: `Astropy` (Astropy Collaboration et al. 2013, 2018, 2022), `CASA` (CASA Team et al. 2022), `matplotlib` (Hunter 2007)

REFERENCES

Adams, F. C., Hollenbach, D., Laughlin, G., & Gorti, U. 2004, ApJ, 611, 360, doi: 10.1086/421989

Alexander, R. D., Clarke, C. J., & Pringle, J. E. 2005, MNRAS, 358, 283, doi: 10.1111/j.1365-2966.2005.08786.x

Anglada, G., Rodríguez, L. F., & Carrasco-González, C. 2018, A&A Rv, 26, 3, doi: 10.1007/s00159-018-0107-z

Anglada, G., Villuendas, E., Estalella, R., et al. 1998, AJ, 116, 2953, doi: 10.1086/300637

Ansdell, M., Williams, J. P., Manara, C. F., et al. 2017, AJ, 153, 240, doi: 10.3847/1538-3881/aa69c0

Ansdell, M., Williams, J. P., Trapman, L., et al. 2018, ApJ, 859, 21, doi: 10.3847/1538-4357/aab890

Aru, M.-L., Mauco, K., Manara, C. F., et al. 2024, arXiv e-prints, arXiv:2403.12604, doi: 10.48550/arXiv.2403.12604

Astropy Collaboration, Robitaille, T. P., Tollerud, E. J., et al. 2013, A&A, 558, A33, doi: 10.1051/0004-6361/201322068

Astropy Collaboration, Price-Whelan, A. M., Sipőcz, B. M., et al. 2018, AJ, 156, 123, doi: 10.3847/1538-3881/aabc4f

Astropy Collaboration, Price-Whelan, A. M., Lim, P. L., et al. 2022, ApJ, 935, 167, doi: 10.3847/1538-4357/ac7c74

Ballering, N. P., Cleeves, L. I., Haworth, T. J., et al. 2023, ApJ, 954, 127, doi: 10.3847/1538-4357/ace901

Bally, J., O'Dell, C. R., & McCaughrean, M. J. 2000, AJ, 119, 2919, doi: 10.1086/301385

Bally, J., Sutherland, R. S., Devine, D., & Johnstone, D. 1998, AJ, 116, 293, doi: 10.1086/300399

Bally, J., Youngblood, A., & Ginsburg, A. 2012, ApJ, 756, 137, doi: 10.1088/0004-637X/756/2/137

Balog, Z., Muzerolle, J., Rieke, G. H., et al. 2007, ApJ, 660, 1532, doi: 10.1086/513311

Baraffe, I., Homeier, D., Allard, F., & Chabrier, G. 2015, A&A, 577, A42, doi: 10.1051/0004-6361/201425481

Beckwith, S. V. W., Sargent, A. I., Chini, R. S., & Guesten, R. 1990, AJ, 99, 924, doi: 10.1086/115385

Berné, O., Habart, É., Peeters, E., et al. 2022, PASP, 134, 054301, doi: 10.1088/1538-3873/ac604c

Berné, O., Habart, E., Peeters, E., et al. 2024, arXiv e-prints, arXiv:2403.00160. https://arxiv.org/abs/2403.00160
Boyden, R. D., & Eisner, J. A. 2020, ApJ, 894, 74, doi: 10.3847/1538-4357/ab86b7
—. 2023, ApJ, 947, 7, doi: 10.3847/1538-4357/acaf77
Carrasco-González, C., Osorio, M., Anglada, G., et al. 2012, ApJ, 746, 71, doi: 10.1088/0004-637X/746/1/71
CASA Team, Bean, B., Bhatnagar, S., et al. 2022, PASP, 134, 114501, doi: 10.1088/1538-3873/ac9642
Cassinelli, J. P., Cohen, D. H., Macfarlane, J. J., et al. 1995, ApJ, 438, 932, doi: 10.1086/175135
Champion, J., Berné, O., Vicente, S., et al. 2017, A&A, 604, A69, doi: 10.1051/0004-6361/201629404
Churchwell, E., Felli, M., Wood, D. O. S., & Massi, M. 1987, ApJ, 321, 516, doi: 10.1086/165648
Clarke, C. J. 2007, MNRAS, 376, 1350, doi: 10.1111/j.1365-2966.2007.11547.x
Coleman, G. A. L., & Haworth, T. J. 2022, MNRAS, 514, 2315, doi: 10.1093/mnras/stac1513
Condon, J. J. 1992, ARA&A, 30, 575, doi: 10.1146/annurev.aa.30.090192.003043
Da Rio, N., Tan, J. C., Covey, K. R., et al. 2016, ApJ, 818, 59, doi: 10.3847/0004-637X/818/1/59
Diaz-Miller, R. I., Franco, J., & Shore, S. N. 1998, ApJ, 501, 192, doi: 10.1086/305793
Dulk, G. A. 1985, ARA&A, 23, 169, doi: 10.1146/annurev.aa.23.090185.001125
Eisner, J. A., Hillenbrand, L. A., Carpenter, J. M., & Wolf, S. 2005, ApJ, 635, 396, doi: 10.1086/497161
Eisner, J. A., Plambeck, R. L., Carpenter, J. M., et al. 2008, ApJ, 683, 304, doi: 10.1086/588524
Eisner, J. A., Arce, H. G., Ballering, N. P., et al. 2018, ApJ, 860, 77, doi: 10.3847/1538-4357/aac3e2
Ercolano, B., Picogna, G., Monsch, K., Drake, J. J., & Preibisch, T. 2021, MNRAS, 508, 1675, doi: 10.1093/mnras/stab2590
Facchini, S., Clarke, C. J., & Bisbas, T. G. 2016, MNRAS, 457, 3593, doi: 10.1093/mnras/stw240
Fang, M., Kim, J. S., Pascucci, I., & Apai, D. 2021, ApJ, 908, 49, doi: 10.3847/1538-4357/abcec8
Fang, M., van Boekel, R., King, R. R., et al. 2012, A&A, 539, A119, doi: 10.1051/0004-6361/201015914
Fang, M., Pascucci, I., Edwards, S., et al. 2018, ApJ, 868, 28, doi: 10.3847/1538-4357/aae780
Fatuzzo, M., & Adams, F. C. 2008, ApJ, 675, 1361, doi: 10.1086/527469
Feigelson, E. D., Carkner, L., & Wilking, B. A. 1998, ApJL, 494, L215, doi: 10.1086/311190
Feigelson, E. D., & Montmerle, T. 1985, ApJL, 289, L19, doi: 10.1086/184426
—. 1999, ARA&A, 37, 363, doi: 10.1146/annurev.astro.37.1.363
Felli, M., Churchwell, E., Wilson, T. L., & Taylor, G. B. 1993a, A&AS, 98, 137
Felli, M., Taylor, G. B., Catarzi, M., Churchwell, E., & Kurtz, S. 1993b, A&AS, 101, 127
Forbrich, J., Rivilla, V. M., Menten, K. M., et al. 2016, ApJ, 822, 93, doi: 10.3847/0004-637X/822/2/93
Gaia Collaboration, Vallenari, A., Brown, A. G. A., et al. 2022, arXiv e-prints, arXiv:2208.00211, doi: 10.48550/arXiv.2208.00211
Garay, G., Moran, J. M., & Reid, M. J. 1987, ApJ, 314, 535, doi: 10.1086/165084
Getman, K. V., Flaccomio, E., Broos, P. S., et al. 2005, ApJS, 160, 319, doi: 10.1086/432092
Großschedl, J. E., Alves, J., Meingast, S., et al. 2018, A&A, 619, A106, doi: 10.1051/0004-6361/201833901
Guarcello, M. G., Prisinzano, L., Micela, G., et al. 2007, A&A, 462, 245, doi: 10.1051/0004-6361:20066124
Guarcello, M. G., Drake, J. J., Wright, N. J., et al. 2016, arXiv e-prints, arXiv:1605.01773, doi: 10.48550/arXiv.1605.01773
Güdel, M. 2002, ARA&A, 40, 217, doi: 10.1146/annurev.astro.40.060401.093806
Gutermuth, R. A., Megeath, S. T., Myers, P. C., et al. 2009, ApJS, 184, 18, doi: 10.1088/0067-0049/184/1/18
Gutermuth, R. A., Myers, P. C., Megeath, S. T., et al. 2008, ApJ, 674, 336, doi: 10.1086/524722
Habart, E., Peeters, E., Berné, O., et al. 2023, arXiv e-prints, arXiv:2308.16732, doi: 10.48550/arXiv.2308.16732
Habing, H. J. 1968, BAN, 19, 421
Hartmann, L., Herczeg, G., & Calvet, N. 2016, ARA&A, 54, 135, doi: 10.1146/annurev-astro-081915-023347
Harvey, P. M., Huard, T. L., Jørgensen, J. K., et al. 2008, ApJ, 680, 495, doi: 10.1086/587687
Haworth, T. J. 2021, MNRAS, 503, 4172, doi: 10.1093/mnras/stab728
Haworth, T. J., & Clarke, C. J. 2019, MNRAS, 485, 3895, doi: 10.1093/mnras/stz706
Haworth, T. J., Clarke, C. J., Rahman, W., Winter, A. J., & Facchini, S. 2018a, MNRAS, 481, 452, doi: 10.1093/mnras/sty2323
Haworth, T. J., Facchini, S., Clarke, C. J., & Mohanty, S. 2018b, MNRAS, 475, 5460, doi: 10.1093/mnras/sty168
Haworth, T. J., Kim, J. S., Winter, A. J., et al. 2021, MNRAS, 501, 3502, doi: 10.1093/mnras/staa3918

Haworth, T. J., Reiter, M., O'Dell, C. R., et al. 2023, MNRAS, 525, 4129, doi: 10.1093/mnras/stad2581
Herczeg, G. J., Najita, J. R., Hillenbrand, L. A., & Pascucci, I. 2007, ApJ, 670, 509, doi: 10.1086/521545
Hildebrand, R. H. 1983, QJRAS, 24, 267
Hillenbrand, L. A. 1997, AJ, 113, 1733, doi: 10.1086/118389
Hirota, T., Bushimata, T., Choi, Y. K., et al. 2007, PASJ, 59, 897, doi: 10.1093/pasj/59.5.897
Hunter, J. D. 2007, Computing in Science and Engineering, 9, 90, doi: 10.1109/MCSE.2007.55
IRSA. 2022, Spitzer Heritage Archive, IPAC, doi: 10.26131/IRSA543
Johnstone, D., Hollenbach, D., & Bally, J. 1998, ApJ, 499, 758, doi: 10.1086/305658
Kim, J. S., Clarke, C. J., Fang, M., & Facchini, S. 2016, ApJL, 826, L15, doi: 10.3847/2041-8205/826/1/L15
Kounkel, M., Hartmann, L., Mateo, M., & Bailey, John I., I. 2017, ApJ, 844, 138, doi: 10.3847/1538-4357/aa7dea
Kounkel, M., Hartmann, L., Loinard, L., et al. 2014, ApJ, 790, 49, doi: 10.1088/0004-637X/790/1/49
Kounkel, M., Covey, K., Suárez, G., et al. 2018, AJ, 156, 84, doi: 10.3847/1538-3881/aad1f1
Kraus, S., Balega, Y. Y., Berger, J. P., et al. 2007, A&A, 466, 649, doi: 10.1051/0004-6361:20066965
Krumholz, M. R., McKee, C. F., & Bland-Hawthorn, J. 2019, ARA&A, 57, 227, doi: 10.1146/annurev-astro-091918-104430
Lada, C. J., & Lada, E. A. 2003, ARA&A, 41, 57, doi: 10.1146/annurev.astro.41.011802.094844
Lada, E. A., Strom, K. M., & Myers, P. C. 1993, in Protostars and Planets III, ed. E. H. Levy & J. I. Lunine, 245
Lang, D., Hogg, D. W., Mierle, K., Blanton, M., & Roweis, S. 2010, AJ, 139, 1782, doi: 10.1088/0004-6256/139/5/1782
Maucó, K., Manara, C. F., Ansdell, M., et al. 2023, A&A, 679, A82, doi: 10.1051/0004-6361/202347627
McCaughrean, M. J., & Pearson, S. G. 2023, arXiv e-prints, arXiv:2310.03552, doi: 10.48550/arXiv.2310.03552
Megeath, S. T., Gutermuth, R., Muzerolle, J., et al. 2012, AJ, 144, 192, doi: 10.1088/0004-6256/144/6/192
Menten, K. M., Reid, M. J., Forbrich, J., & Brunthaler, A. 2007, A&A, 474, 515, doi: 10.1051/0004-6361:20078247
Mezger, P. G., & Henderson, A. P. 1967, ApJ, 147, 471, doi: 10.1086/149030
Mooley, K., Hillenbrand, L., Rebull, L., Padgett, D., & Knapp, G. 2013, ApJ, 771, 110, doi: 10.1088/0004-637X/771/2/110
Natta, A., Testi, L., Alcalá, J. M., et al. 2014, A&A, 569, A5, doi: 10.1051/0004-6361/201424136
Ndugu, N., Bitsch, B., & Jurua, E. 2018, MNRAS, 474, 886, doi: 10.1093/mnras/stx2815
Nicholson, R. B., Parker, R. J., Church, R. P., et al. 2019, MNRAS, 485, 4893, doi: 10.1093/mnras/stz606
O'Dell, C. R., & Beckwith, S. V. W. 1997, Science, 276, 1355, doi: 10.1126/science.276.5317.1355
O'Dell, C. R., Kollatschny, W., & Ferland, G. J. 2017, ApJ, 837, 151, doi: 10.3847/1538-4357/aa6198
O'dell, C. R., & Wen, Z. 1994, ApJ, 436, 194, doi: 10.1086/174892
Otter, J., Ginsburg, A., Ballering, N. P., et al. 2021, ApJ, 923, 221, doi: 10.3847/1538-4357/ac29c2
Owen, J. E., Clarke, C. J., & Ercolano, B. 2012, MNRAS, 422, 1880, doi: 10.1111/j.1365-2966.2011.20337.x
Owen, J. E., Scaife, A. M. M., & Ercolano, B. 2013, MNRAS, 434, 3378, doi: 10.1093/mnras/stt1254
Panagia, N., & Felli, M. 1975, A&A, 39, 1
Parker, R. J., Alcock, H. L., Nicholson, R. B., Panić, O., & Goodwin, S. P. 2021a, ApJ, 913, 95, doi: 10.3847/1538-4357/abf4cc
Parker, R. J., Nicholson, R. B., & Alcock, H. L. 2021b, MNRAS, 502, 2665, doi: 10.1093/mnras/stab054
Pascucci, I., Cabrit, S., Edwards, S., et al. 2022, arXiv e-prints, arXiv:2203.10068, doi: 10.48550/arXiv.2203.10068
Pascucci, I., Gorti, U., & Hollenbach, D. 2012, ApJL, 751, L42, doi: 10.1088/2041-8205/751/2/L42
Pascucci, I., Ricci, L., Gorti, U., et al. 2014, ApJ, 795, 1, doi: 10.1088/0004-637X/795/1/1
Peterson, D. E., & Megeath, S. T. 2008, in Handbook of Star Forming Regions, Volume I, ed. B. Reipurth, Vol. 4, 590, doi: 10.48550/arXiv.0809.4006
Picogna, G., Ercolano, B., Owen, J. E., & Weber, M. L. 2019, MNRAS, 487, 691, doi: 10.1093/mnras/stz1166
Plambeck, R. L., Wright, M. C. H., Mundy, L. G., & Looney, L. W. 1995, ApJL, 455, L189, doi: 10.1086/309830
Qiao, L., Coleman, G. A. L., & Haworth, T. J. 2023, MNRAS, 522, 1939, doi: 10.1093/mnras/stad944
Qiao, L., Haworth, T. J., Sellek, A. D., & Ali, A. A. 2022, MNRAS, 512, 3788, doi: 10.1093/mnras/stac684
Rau, U., & Cornwell, T. J. 2011, A&A, 532, A71, doi: 10.1051/0004-6361/201117104
Reipurth, B., Rodríguez, L. F., & Chini, R. 1999, AJ, 118, 983, doi: 10.1086/300958
Reynolds, S. P. 1986, ApJ, 304, 713, doi: 10.1086/164209
Ricci, L., Robberto, M., & Soderblom, D. R. 2008, AJ, 136, 2136, doi: 10.1088/0004-6256/136/5/2136
Rodriguez, L. F., Canto, J., Torrelles, J. M., et al. 1994, ApJL, 427, L103, doi: 10.1086/187375

Rodriguez, L. F., Myers, P. C., Cruz-Gonzalez, I., & Terebey, S. 1989, ApJ, 347, 461, doi: 10.1086/168134
Sanchis, E., Testi, L., Natta, A., et al. 2021, A&A, 649, A19, doi: 10.1051/0004-6361/202039733
Sandstrom, K. M., Peek, J. E. G., Bower, G. C., Bolatto, A. D., & Plambeck, R. L. 2007, ApJ, 667, 1161, doi: 10.1086/520922
Scally, A., & Clarke, C. 2001, MNRAS, 325, 449, doi: 10.1046/j.1365-8711.2001.04274.x
Sellek, A. D., Booth, R. A., & Clarke, C. J. 2020, MNRAS, 492, 1279, doi: 10.1093/mnras/stz3528
Sheehan, P. D., Eisner, J. A., Mann, R. K., & Williams, J. P. 2016, ApJ, 831, 155, doi: 10.3847/0004-637X/831/2/155
Sheehan, P. D., Tobin, J. J., Looney, L. W., & Megeath, S. T. 2022, ApJ, 929, 76, doi: 10.3847/1538-4357/ac574d
Shkolnik, E. L., & Barman, T. S. 2014, AJ, 148, 64, doi: 10.1088/0004-6256/148/4/64
Smith, N., Bally, J., Licht, D., & Walawender, J. 2005, AJ, 129, 382, doi: 10.1086/426567
Smith, N., Bally, J., & Walborn, N. R. 2010, MNRAS, 405, 1153, doi: 10.1111/j.1365-2966.2010.16520.x
Störzer, H., & Hollenbach, D. 1999, ApJ, 515, 669, doi: 10.1086/307055
Throop, H. B., & Bally, J. 2005, ApJL, 623, L149, doi: 10.1086/430272
Tobin, J. J., Sheehan, P. D., Megeath, S. T., et al. 2020, ApJ, 890, 130, doi: 10.3847/1538-4357/ab6f64
Tychoniec, Ł., Tobin, J. J., Karska, A., et al. 2018a, ApJ, 852, 18, doi: 10.3847/1538-4357/aa9980
—. 2018b, ApJS, 238, 19, doi: 10.3847/1538-4365/aaceae
van Terwisga, S. E., & Hacar, A. 2023, A&A, 673, L2, doi: 10.1051/0004-6361/202346135
van Terwisga, S. E., Hacar, A., & van Dishoeck, E. F. 2019, A&A, 628, A85, doi: 10.1051/0004-6361/201935378
van Terwisga, S. E., van Dishoeck, E. F., Mann, R. K., et al. 2020, A&A, 640, A27, doi: 10.1051/0004-6361/201937403
Vargas-González, J., Forbrich, J., Dzib, S. A., & Bally, J. 2021, MNRAS, 506, 3169, doi: 10.1093/mnras/stab1826
Walsh, C., Millar, T. J., & Nomura, H. 2013, ApJL, 766, L23, doi: 10.1088/2041-8205/766/2/L23
Wendker, H. J., Baars, J. W. M., & Altenhoff, W. J. 1973, Nature Physical Science, 245, 118, doi: 10.1038/physci245118a0
Winter, A. J., Clarke, C. J., Rosotti, G., et al. 2018, MNRAS, 478, 2700, doi: 10.1093/mnras/sty984
Winter, A. J., Clarke, C. J., Rosotti, G. P., Hacar, A., & Alexander, R. 2019, MNRAS, 490, 5478, doi: 10.1093/mnras/stz2545
Winter, A. J., & Haworth, T. J. 2022, European Physical Journal Plus, 137, 1132, doi: 10.1140/epjp/s13360-022-03314-1
Winter, A. J., Haworth, T. J., Coleman, G. A. L., & Nayakshin, S. 2022, MNRAS, 515, 4287, doi: 10.1093/mnras/stac1564
Winter, A. J., Kruijssen, J. M. D., Longmore, S. N., & Chevance, M. 2020, Nature, 586, 528, doi: 10.1038/s41586-020-2800-0
Wright, A. E., & Barlow, M. J. 1975, MNRAS, 170, 41, doi: 10.1093/mnras/170.1.41
Zapata, L. A., Rodríguez, L. F., Kurtz, S. E., & O'Dell, C. R. 2004a, AJ, 127, 2252, doi: 10.1086/382715
Zapata, L. A., Rodríguez, L. F., Kurtz, S. E., O'Dell, C. R., & Ho, P. T. P. 2004b, ApJL, 610, L121, doi: 10.1086/423428

APPENDIX

A. BACKGROUND SOURCE DETECTIONS

Here we discuss the radio flux measurements, continuum images, and SEDs for the 37 VLA detections that we classify as probable background objects. In Table 5, we list the source IDs, coordinates, radio flux measurements, and radio spectral indices for each background source. The radio spectral indices are measured by fitting a single power law to the measured 3.0, 6.4, and 15.0 GHz fluxes. Table 5 also indicates whether a background source is a known radio source from the Kounkel et al. (2014) catalog, as well as whether the detected emission is resolved, circularly polarized, and/or variable.

In general, the sample of candidate background sources that we have identified from our infrared photometric selection criteria (see Section 2) is consistent with the expected distribution of background radio sources in our VLA maps. Following Rodriguez et al. (1989), the number of background radio sources per square degree with a flux greater than or equal to S_ν can be estimated via the equation

$$\langle N \rangle = 40 \left(\frac{S_\nu}{\mathrm{mJy}} \right)^{-0.75} \mathrm{deg}^{-2}. \quad \text{(A1)}$$

The top panel of Figure 15 compares the flux distributions of our sample of probable background sources with the distribution obtained for our full sample of 46 unclassified radio-detected sources (i.e., detections not associated with a proplyd or YSO catalog), and the distribution predicted from Equation A1 for a field size of $\sim 25' \times 25'$. The bottom panel of Figure 3 shows the spatial distribution of background sources compared with both the spatial distribution of the unclassified radio sources and the predicted spatial distribution for detected background radio sources in our VLA maps. These figures reveal that both the flux and spatial distributions of the candidate background sources match up well with the predicted distributions from Equation A1, particularly towards the brighter end of the flux distribution and the outskirts of our maps, where all detections are consistent with being background objects. They also demonstrate that a subset of the faint (< 1 mJy) unclassified detections within $\sim 10'$ of 42 Ori are likely newly-identified cluster members of NGC 1977, rather than additional background sources.

In Figures 16 - 21, we show the 3.0 GHz subimages, 6.4 GHz subimages, 15.0 GHz subimages, and radio SEDs for each background object using a similar layout as in Figure 4. In the SED panels of Figures 16 - 21, we also include the best-fit power law and 1σ confidence intervals derived for each background source (see Section 4.2).

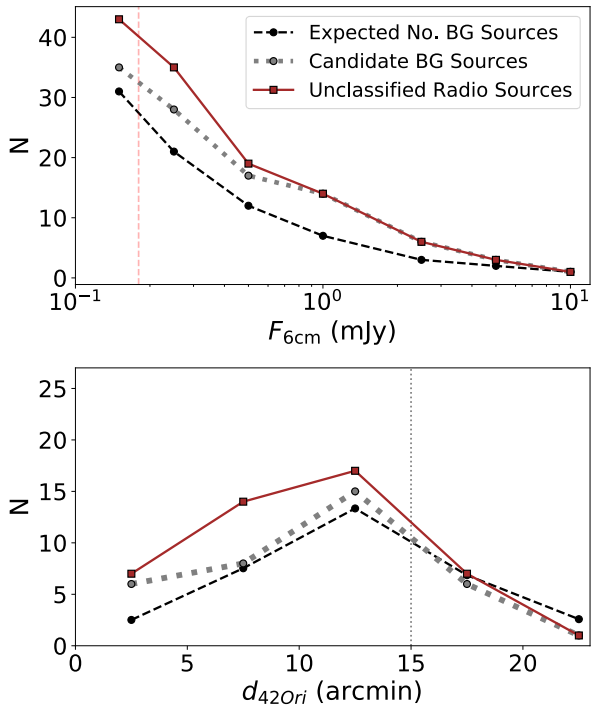

Figure 15. Top: Cumulative number of unclassified radio sources (brown) and candidate background sources (gray) detected above a certain flux level, compared with the expected number of background sources within the central $25'$ region of NGC 1977 (black). Unclassified radio sources consist of the 46 detections that are not associated with the proplyd or YSO catalogs assembled in Section 2. The red dashed line depicts the typical 6σ rms level in our VLA maps. Bottom: Radially-averaged spatial distribution of the unclassified radio sources and candidate background sources, compared with the predicted number of background radio sources in our VLA maps with fluxes greater than the local 6σ rms level.

Many of the candidate background objects have steep negative radio spectral indices that are much lower than the values expected for optically thin or optically thick free-free emission (e.g., sources B9, B14, B22, and B26). These background objects are likely to be emitting strong levels of non-thermal emission, such as gyrosynchrotron emission (e.g., Feigelson & Montmerle 1999). This is expected for extragalactic radio sources, as the radio SEDs of galaxies are known to be dominated by gyrosynchrotron radiation under a range of physical conditions (Condon 1992, and references therein).

We also find that a subset of background sources shown in Figures 16 - 21 has flat spectra that are consis-

tent with optically thin free-free emission (e.g., sources B6, B16, and B23). Star-forming galaxies can, at times, exhibit flat radio spectra that spectrally resemble optically thin free-free emission (see review in Condon 1992), so it seems reasonable for some of the background objects detected in our maps to be fit well by flat-sloped power laws even if they are extragalactic.

Table 5. Properties of background radio sources detected in our VLA maps

ID	R.A. (J2000)	Decl. (J2000)	Catalog	$F_{\nu,\ 3.0\ \mathrm{GHz}}$ (mJy)	$F_{\nu,\ 6.4\ \mathrm{GHz}}$ (mJy)	$F_{\nu,\ 15.0\ \mathrm{GHz}}$ (mJy)	Sp. Index	Res.?	Pol.?	Var.?
(1)	(2)	(3)	(4)	(5)	(6)	(7)	(8)	(9)	(10)	(11)
B1	05:36:08.64	–4:34:45.40	···	5.231 ± 0.379	6.015 ± 0.431	···	$0.18^{0.14}_{0.10}$		Y	
B2	05:36:23.36	–4:37:04.83	···	11.272 ± 0.801	4.061 ± 0.304	···	$-1.36^{0.14}_{0.10}$	Y	Y	
B3	05:35:21.84	–4:37:59.30	K14	1.992 ± 0.148	1.269 ± 0.093	3.031 ± 5.080	$-0.59^{0.14}_{0.14}$	Y		
B4	05:35:50.28	–4:39:32.60	K14	0.917 ± 0.075	0.665 ± 0.052	2.463 ± 10.005	$-0.42^{0.14}_{0.17}$			
B5	05:36:03.67	–4:40:30.80	K14	0.602 ± 0.055	1.414 ± 0.103	2.481 ± 0.185	$0.84^{0.07}_{0.04}$			
B6	05:35:30.52	–4:40:35.99	···	0.169 ± 0.036	0.177 ± 0.025	0.196 ± 0.038	$0.11^{0.25}_{0.28}$			
B7	05:34:28.70	–4:40:38.61	···	0.328 ± 0.069	0.308 ± 0.041	···	$-0.07^{0.49}_{0.46}$			
B8	05:36:25.10	–4:41:51.57	···	1.554 ± 0.122	1.378 ± 0.106	46.165 ± 112.296	$-0.17^{0.18}_{0.14}$	Y		
B9	05:35:50.63	–4:42:02.00	K14	2.793 ± 0.200	1.774 ± 0.127	0.673 ± 0.068	$-0.84^{0.07}_{0.07}$	Y		
B10	05:36:09.39	–4:42:53.65	···	0.252 ± 0.038	0.172 ± 0.026	-0.037 ± 0.221	$-0.52^{0.35}_{0.38}$			
B11	05:35:35.97	–4:43:41.24	···	0.218 ± 0.034	0.164 ± 0.025	0.012 ± 0.137	$-0.42^{0.35}_{0.38}$			
B12	05:34:30.54	–4:44:29.40	K14	0.604 ± 0.062	0.765 ± 0.059	63.094 ± 184.289	$0.32^{0.21}_{0.21}$			Y
B13	05:34:31.50	–4:44:42.87	···	0.088 ± 0.150	0.181 ± 0.027	0.713 ± 78.576	> -0.77			
B14	05:36:23.14	–4:44:59.60	K14	2.100 ± 0.155	1.018 ± 0.079	···	$-0.94^{0.14}_{0.14}$	Y		Y
B15	05:34:36.52	–4:45:18.40	···	0.041 ± 0.130	0.239 ± 0.028	4.019 ± 9.329	>0.04			
B16	05:34:50.92	–4:47:04.45	···	0.162 ± 0.031	0.155 ± 0.023	0.220 ± 0.203	$-0.03^{0.46}_{0.42}$			
B17	05:36:11.72	–4:47:07.00	K14	0.868 ± 0.072	1.506 ± 0.109	0.839 ± 2.495	$0.70^{0.17}_{0.14}$			
B18	05:35:17.81	–4:48:03.49	···	0.403 ± 0.041	0.303 ± 0.032	0.156 ± 0.242	$-0.38^{0.25}_{0.25}$	Y		
B19	05:35:07.24	–4:48:53.20	K14	0.297 ± 0.036	0.411 ± 0.036	0.241 ± 0.046	$-0.03^{0.10}_{0.14}$			
B20	05:35:14.70	–4:49:05.49	···	0.132 ± 0.030	0.160 ± 0.025	0.118 ± 0.145	$0.18^{0.46}_{0.46}$		Y	
B21	05:35:47.43	–4:49:52.60	K14	1.935 ± 0.142	1.608 ± 0.116	0.462 ± 0.049	$-0.80^{0.04}_{0.07}$			
B22	05:35:47.56	–4:49:53.30	K14	1.943 ± 0.143	1.491 ± 0.108	0.472 ± 0.049	$-0.80^{0.04}_{0.07}$		Y	
B23	05:35:31.03	–4:50:38.40	K14	0.362 ± 0.040	0.469 ± 0.040	0.301 ± 0.042	$-0.07^{0.10}_{0.10}$		Y	
B24	05:35:58.42	–4:51:23.19	···	0.272 ± 0.040	0.272 ± 0.032	-0.079 ± 1.320	$0.00^{0.35}_{0.31}$			
B25	05:35:13.90	–4:51:59.30	K14	2.290 ± 0.165	0.974 ± 0.076	0.218 ± 0.063	$-1.26^{0.10}_{0.10}$	Y	Y	
B26	05:35:13.73	–4:52:01.90	K14	12.769 ± 0.904	8.419 ± 0.596	2.011 ± 0.154	$-1.15^{0.07}_{0.04}$	Y	Y	
B27	05:35:57.91	–4:52:32.44	···	0.325 ± 0.041	0.330 ± 0.038	0.457 ± 1.435	$0.04^{0.28}_{0.31}$			
B28	05:34:24.63	–4:53:03.84	···	2.693 ± 0.196	2.688 ± 0.193	-1.957 ± 7.527	$0.00^{0.14}_{0.14}$	Y	Y	
B29	05:34:19.75	–4:53:22.31	···	0.425 ± 0.062	0.446 ± 0.047	18.413 ± 88.576	$0.07^{0.31}_{0.31}$	Y		
B30	05:36:14.03	–4:53:29.38	···	0.397 ± 0.047	0.658 ± 0.057	2.285 ± 13.865	$0.66^{0.25}_{0.24}$			
B31	05:36:13.78	–4:54:40.13	···	0.273 ± 0.044	0.328 ± 0.045	···	$0.25^{0.39}_{0.39}$			
B32[a]	05:35:58.88	–4:55:37.70	K14	25.922 ± 1.833	61.653 ± 4.361	63.940 ± 4.544	$0.56^{0.04}_{0.04}$		Y	
B33	05:36:11.91	–4:56:34.14	···	0.535 ± 0.054	0.468 ± 0.057	···	$-0.17^{0.25}_{0.28}$			
B34	05:35:00.69	–4:57:53.50	K14	4.521 ± 0.322	2.955 ± 0.211	0.862 ± 0.111	$-0.91^{0.07}_{0.07}$	Y	Y	
B35	05:36:04.43	–4:59:08.40	K14	0.315 ± 0.050	0.435 ± 0.057	-56.370 ± 111.789	$0.42^{0.39}_{0.35}$		Y	Y
B36	05:35:37.21	–5:00:55.20	K14	0.097 ± 0.198	0.372 ± 0.053	···	> -0.1			
B37	05:35:55.90	–5:04:25.20	K14	0.406 ± 0.087	···	···	···			

Notes. Column (1): source IDs used in this article. Columns (2) and (3): phase center coordinates. Column (3): catalog association of VLA-detected sources. Here we use the same notation as in Table 3. Columns (5), (6), and (7): measured fluxes at 3.0 GHz, 6.4 GHz, and 15.0 GHz. Column (8): Best-fit spectral index derived from fitting a power law to the measued radio fluxes. Column (9): Source morphology tracker. A 'Y' is used to denote sources that are spatially resolved in one or more bands. Empty entries indicate detections that are unresolved in our VLA maps. Column (10): Circular polarization indicator. A 'Y' denotes a source with Stokes V emission detected above a 2.5σ level. Column (11): Variable source indicator. A 'Y' is used to denote sources with variable ∼6.4 GHz emission, based on comparisons with prior flux measurements from Kounkel et al. (2014) (see Section 4.4).

[a]Indicates the bright radio source J053558.88-045537.7

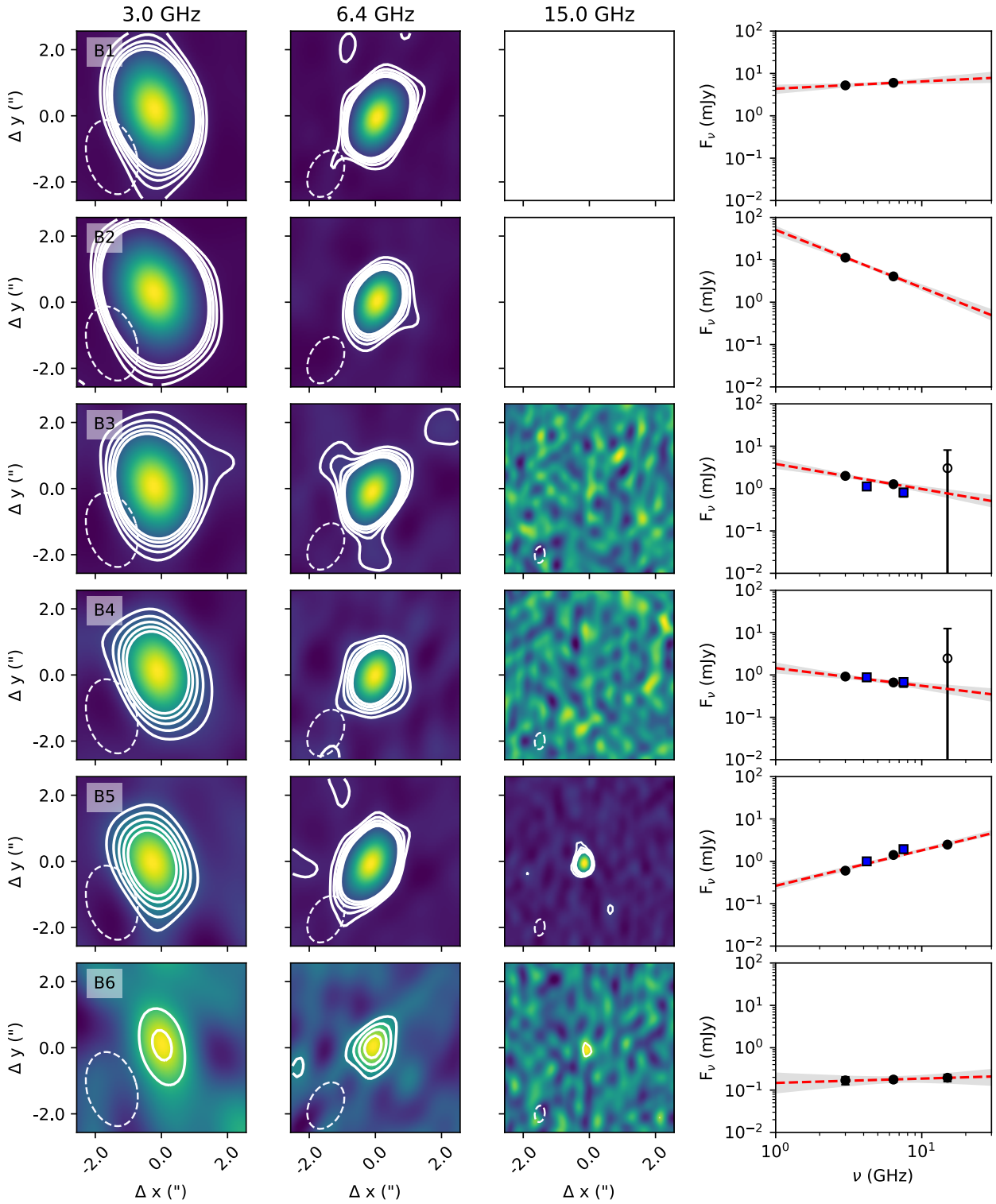

Figure 16. Same as Figure 4, but for background objects detected in our VLA maps. For sources that lie outside of the field of views of our 6.4 GHz and/or 15.0 GHz observations (see Figure 1), we use whitespace to fill in the corresponding image subpanels.

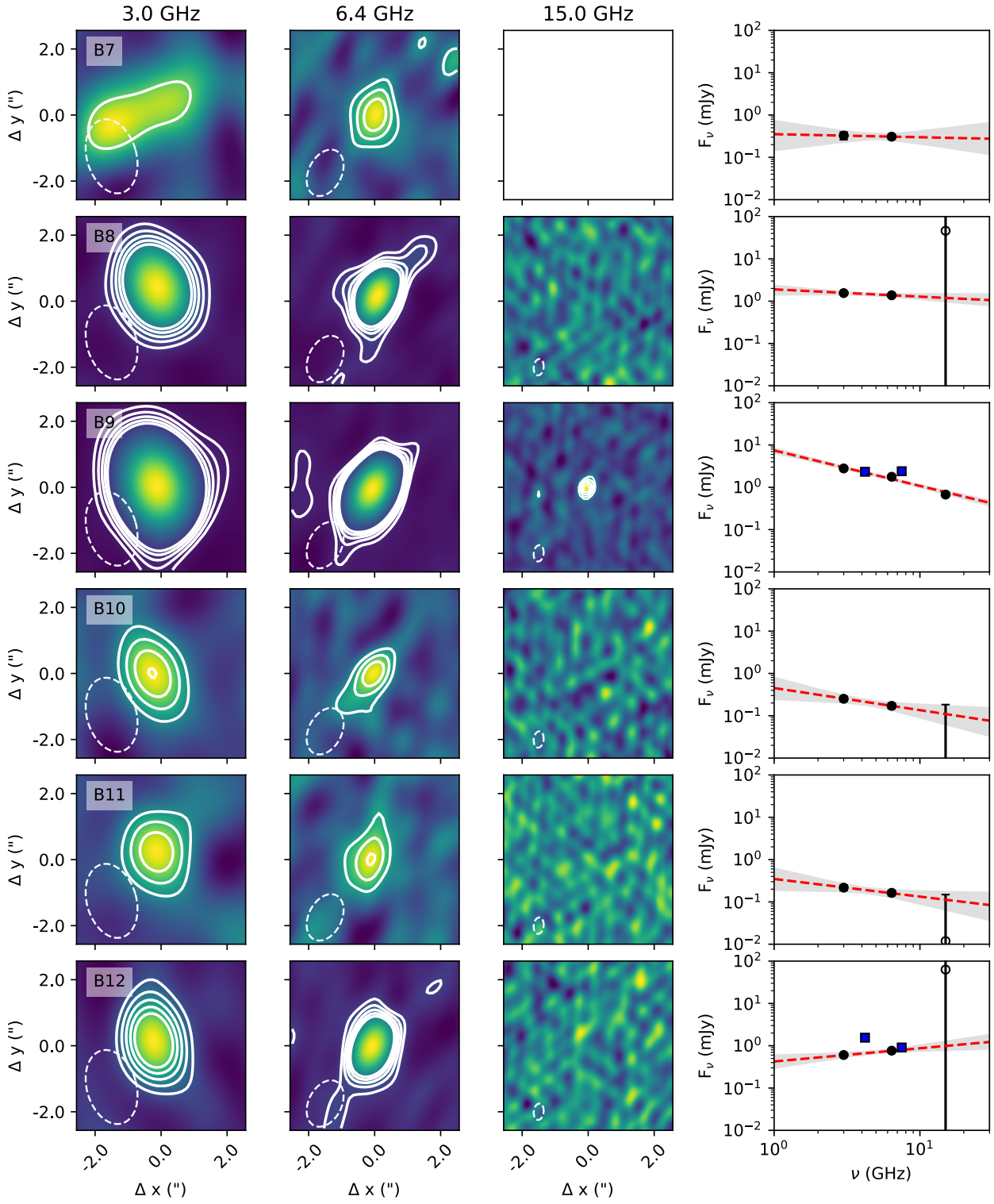

Figure 17. Continuation of Figure 16.

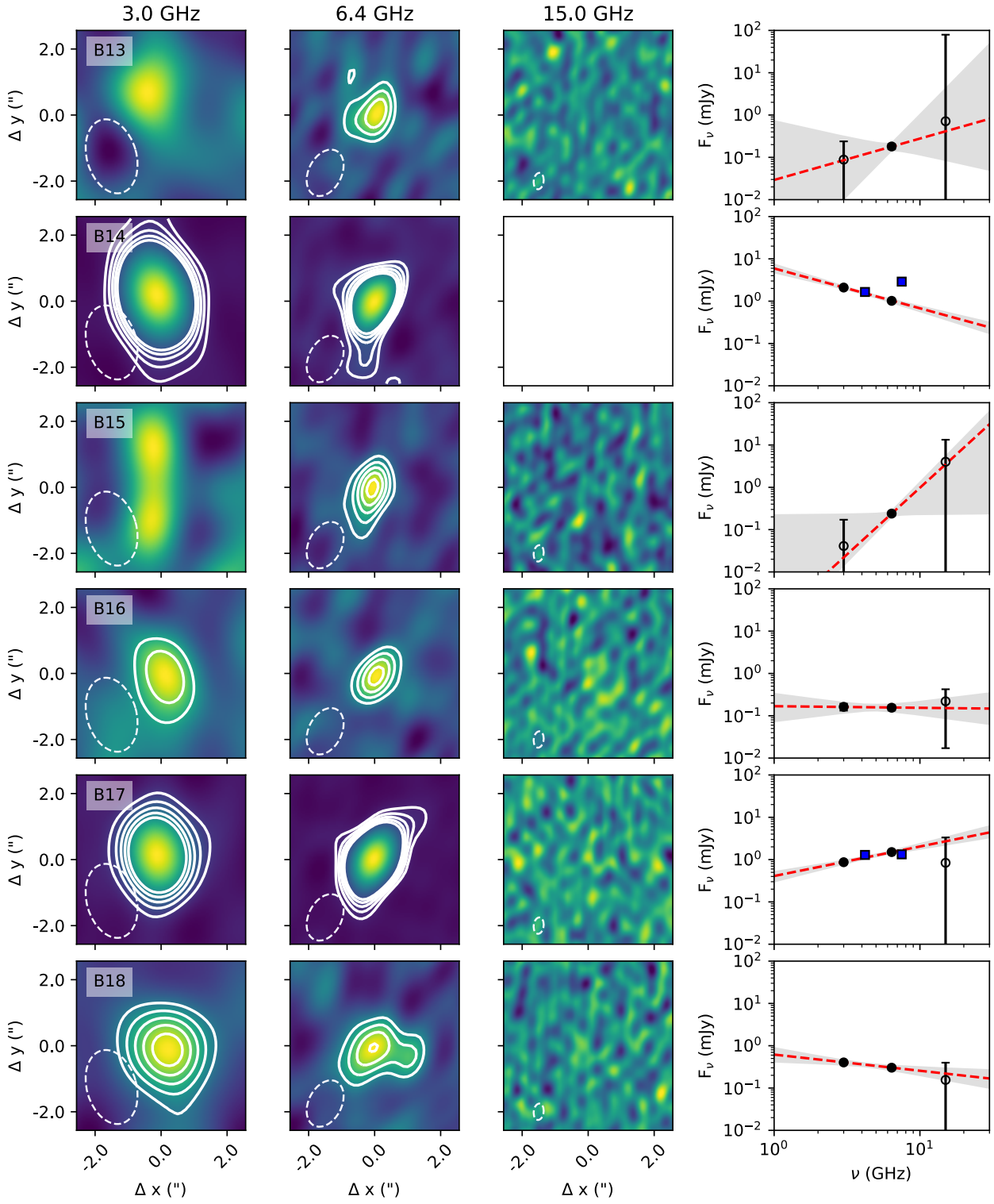

Figure 18. Continuation of Figure 16.

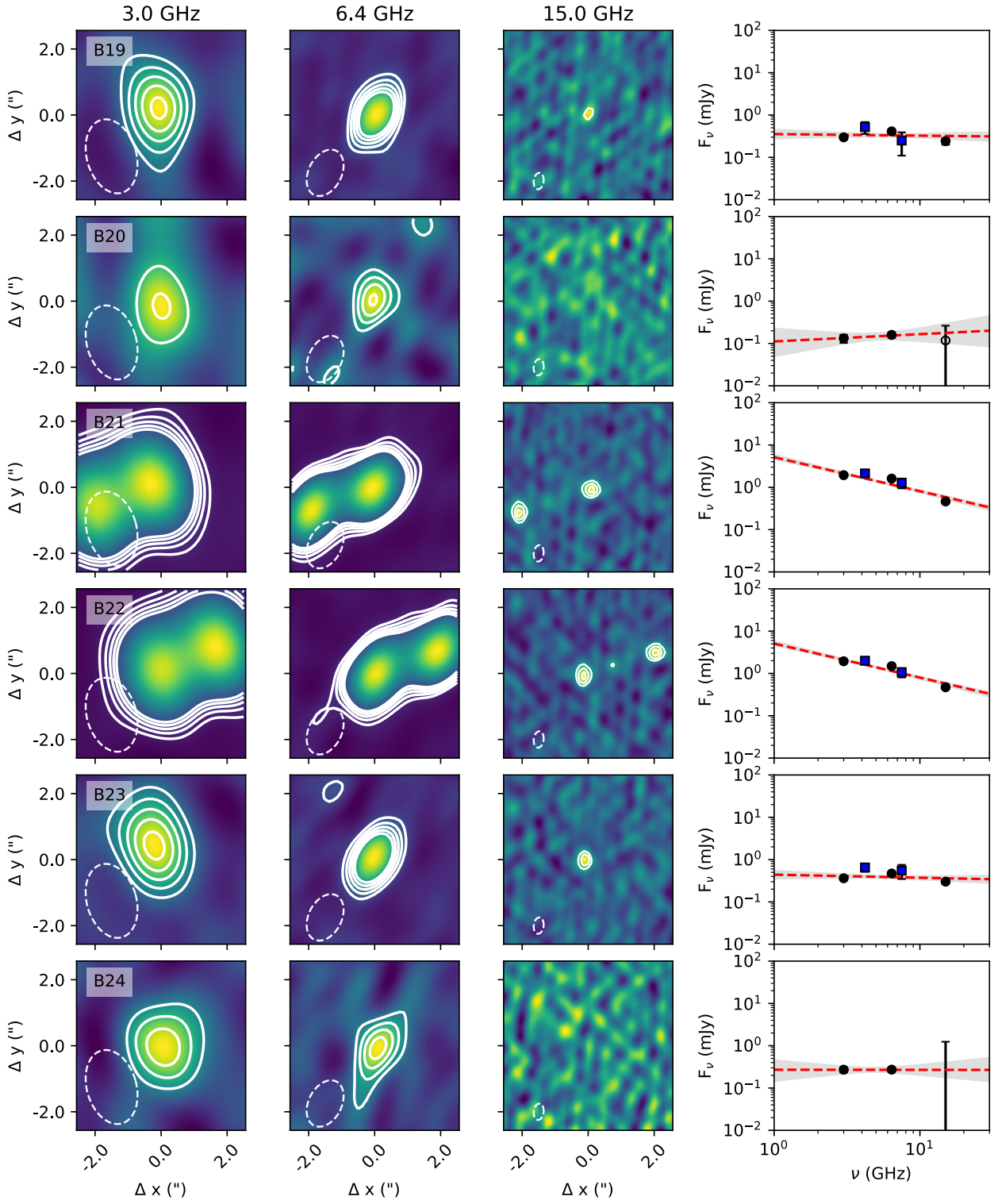

Figure 19. Continuation of Figure 16.

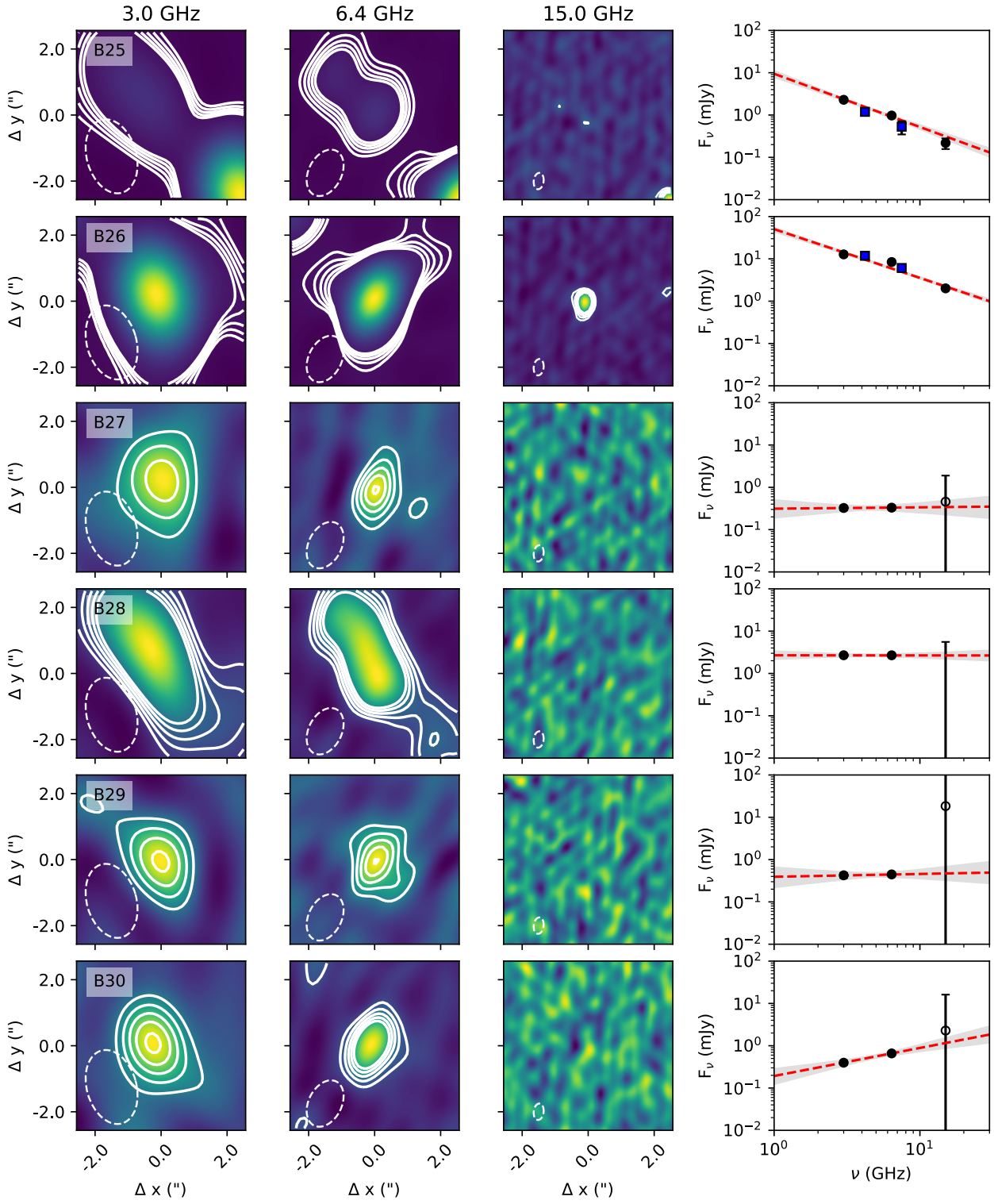

Figure 20. Continuation of Figure 16.

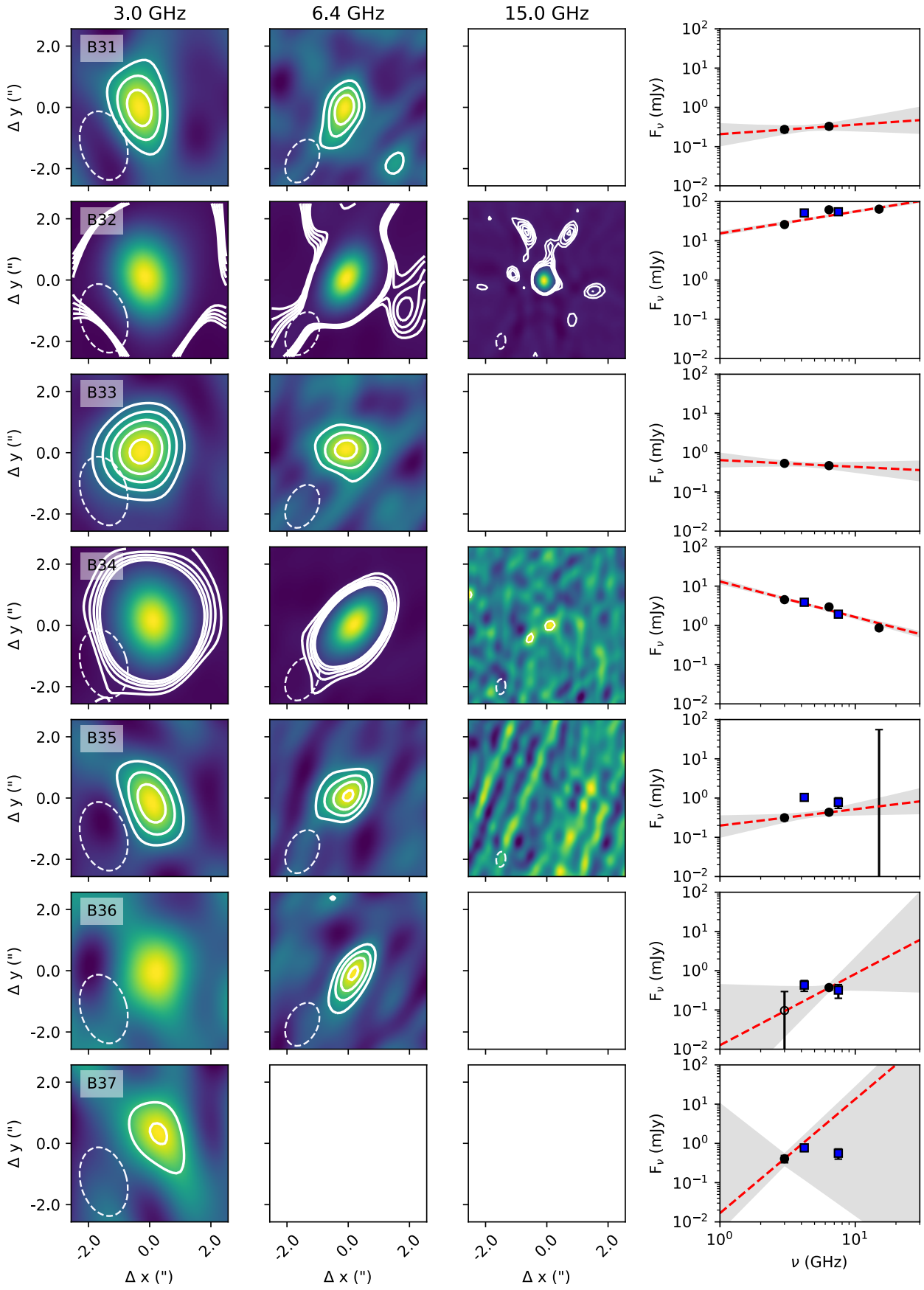

Figure 21. Continuation of Figure 16.